Journal of Volcanology and Geothermal Research 351 (2018) 57–74

Contents lists available at ScienceDirect

Journal of Volcanology and Geothermal Research

journal homepage: www.elsevier.com/locate/jvolgeores

Magma wagging and whirling in volcanic conduits

Yang Liao[a,*,1], David Bercovici[a], Mark Jellinek[b]

[a] *Department of Geology & Geophysics, Yale University, New Haven, Connecticut, USA*
[b] *Department of Earth, Ocean & Atmosphere, University of British Columbia, Vancouver, BC, Canada*

ARTICLE INFO

Article history:
Received 2 September 2016
Received in revised form 20 November 2017
Accepted 20 December 2017
Available online 29 December 2017

Keywords:
Volcanic tremor
Magma dynamics
Volcano seismology

ABSTRACT

Seismic tremor characterized by 0.5–7 Hz ground oscillations commonly occur before and during eruptions at silicic volcanoes with widely ranging vent geometries and edifice structures. The ubiquitous characteristics of this tremor imply that its causes are potentially common to silicic volcanoes. Here we revisit and extend to three dimensions the magma-wagging model for tremor (Jellinek and Bercovici, 2011; Bercovici et al., 2013), wherein a stiff magma column rising in a vertical conduit oscillates against a surrounding foamy annulus of bubbly magma, giving rise to tremor. While prior studies were restricted to two-dimensional lateral oscillations, here we explore three-dimensional motion and additional modes of oscillations. In the absence of viscous damping, the magma column undergoes 'whirling' motion: the center of each horizontal section of the column traces an elliptical trajectory. In the presence of viscous effect we identify new 'coiling' and 'uncoiling' column bending shapes with relatively higher and comparable rates of dissipation to the original two-dimensional magma wagging model. We also calculate the seismic P-wave response of the crustal material around the volcanic conduit to the new whirling motions and propose seismic diagnostics for different wagging patterns using the time-lag between seismic stations. We test our model by analyzing pre-eruptive seismic data from the 2009 eruption of Redoubt Volcano. In addition to suggesting that the occurrence of elliptical whirling motion more than 1 week before the eruption, our analysis of seismic time-lags also implies that the 2009 eruption was accompanied by qualitative changes in the magma wagging behavior including fluctuations in eccentricity and a reversal in the direction of elliptical whirling motion when the eruption was immediately impending.

1. Introduction

Volcanic tremor is a common feature of explosive volcanism and plays an important role in volcanic hazard monitoring and eruption forecasting. Typically, a tremor emerges with frequencies of 0.5 to 2 Hz several hours to days before the eruption starts. As the volcano's activity intensifies, frequencies can glide up, increasing to 5 to 7 Hz (Thompson et al., 2002; Neuberg, 2000; Konstantinou and Schlindwein, 2003; McNutt, 2005; McNutt and Nishimura, 2008; Chouet and Matoza, 2013; Unglert and Jellinek, 2017). An understanding of the origin of volcanic tremor and an explanation for the full range of behaviors of pre-eruptive tremor may consequently be key for forecasting dangerous explosive volcanism.

There are several important aspects of volcanic tremor, including its frequency range, its emergence and temporal evolution in frequency and amplitude, and the longevity of the tremor signal. Many tremor models are developed to explain one or more of these aspects. For example, the range of frequencies around 1 Hz can be explained either by stirring of the gas-magma mixture and wave excitement (Garcés et al., 1998), 'wagging' of the magma column (Jellinek and Bercovici, 2011), or possibly fluids passing through elastic channels or cracks (Rust et al., 2008). The emergence and longevity of tremor can be explained by accounting for transport of magma through a constricted crack in the conduit (Julian, 1994; Chouet, 1988), as well as by gas flux forcing of magma column oscillations (Bercovici et al., 2013). The gliding of tremor frequency when approaching eruption can be explained by a stick-slip model (Hotovec et al., 2013; Dmitrieva et al., 2013), by gas-magma stirring (Garcés et al., 1998), and possibly by thinning and destruction of the vesicular annulus surrounding the magma column (Jellinek and Bercovici, 2011). Some of these models explain additional features associated with tremor; for example, Garcés et al. (1998)account for the relationship between seismicity and infrasound measurements. The recently

---

[*] Corresponding author.
E-mail address: yliao@whoi.edu (Y. Liao).

[1] Now at Department of Geology & Geophysics, Woods Hole Oceanographic Institution, Falmouth, Massachusetts, USA.

https://doi.org/10.1016/j.jvolgeores.2017.12.016
0377-0273/© 2017 Published by Elsevier B.V.

observed correlation between tremor and degassing (Nadeau et al., 2011) is possibly explained by the extended magma-wagging model (Bercovici et al., 2013).

Apart from the frequency content, the spatial variation of the tremor's seismic signal is also a measurable quantity, given an array of seismometers, and likely provides further characteristics of tremor activity. For example, radiation patterns of the seismic signal emanating from the source (e.g., whether circular, helical or dipolar) indicate the polarity of the tremor source. The evolution of this spatial structure en route to an eruption may provide another unique feature of tremor activity. Bercovici et al. (2013) explored the seismic spatial structure by studying cross-correlation of seismic signals measured at two stations across a conduit, and could account for the time-lag between the two signals with their magma wagging model. However, this magma wagging model (Jellinek and Bercovici, 2011; Bercovici et al., 2013) limits the motion of the magma column to a two-dimensional (2-D) plane, which yields a seismic radiation pattern that is dipolar, with the axis of symmetry along the wagging direction. Here we propose an extended magma wagging model that relaxes the 2-D constraint, and with which we can explore the spatial and temporal features of the seismic radiation pattern associated with tremor.

The 2-D magma wagging model (Jellinek and Bercovici, 2011) is based on the assumption that, inside the volcanic conduit, the magma column is enveloped by a gas-rich foamy annulus. When the magma column is displaced to one side of the conduit, the bubbles in the annulus become compressed, and their increased gas pressure pushes the magma column back towards its resting position, although it overshoots, thereby triggering oscillations from side to side in the conduit. When the annulus contains isolated bubbles filled with ideal gas, the system acts like a simple mass oscillator between two springs. The fundamental angular frequency for free-oscillations of the magma column is

$$\omega_o = \sqrt{\frac{2\rho_o C_g^2}{\Phi_o \rho_m (R_c^2 - R_m^2)}} \tag{1}$$

where ρ_o and Φ_o are the undisturbed gas density and gas volume fraction in the annulus, C_g is the isothermal sound speed in the gas, ρ_m is the magma density and R_m and R_c are the radii of the magma column and conduit, respectively (see Fig. 1).

The magma wagging model requires the knowledge of gas density, sound speed and conduit radius, which can be estimated from laboratory measurements of gas properties and field observations of volcanic structure. Moreover, the tremor frequency predicted by Eq. (1) is weakly dependent on these quantities: for a reasonably wide range of conduit properties, Eq. (1) predicts an ordinary wagging frequency $\omega_o/(2\pi)$ between about 0.1 Hz and 5 Hz, similar to the observed range of tremor frequencies (Jellinek and Bercovici, 2011). Bercovici et al. (2013) extends the original magma-wagging model by adding permeability to the annulus and allowing gas flow through the interconnected tube-like bubbles in the vertical direction. The extended model shows that the gas flux leads to a Bernoulli force driving mechanism that can excite wagging motion. The magma-wagging models are successful in explaining the ubiquity, persistence and temporal behavior of pre- and syn-eruptive volcanic tremor observed at a number of volcanoes. However, in these first applications of the 2-D magma wagging model, motion and deformation of the magma column are confined to be in the same direction. These applications therefore preclude any angular velocity or relative angular displacement of the magma column, which could potentially cause additional tremor frequencies or indicate rotational characteristics evolving on route to an eruption. The lateral motion associated with the non-vanishing angular velocity of the magma column could induce more features in the spatial variation of seismic radiation pattern as well. Here, we extend the original magma-wagging model to three dimensions by introducing angular motion of the magma column. We present a model for the three dimensional motion of the magma column in Section 2. Analytical and numerical analysis of the nonlinear wagging motions will be presented in Sections 3 and 4. The seismic radiation pattern triggered by the wagging motions will be presented in Section 5, and applications to volcano seismology will be discussed in Section 6.

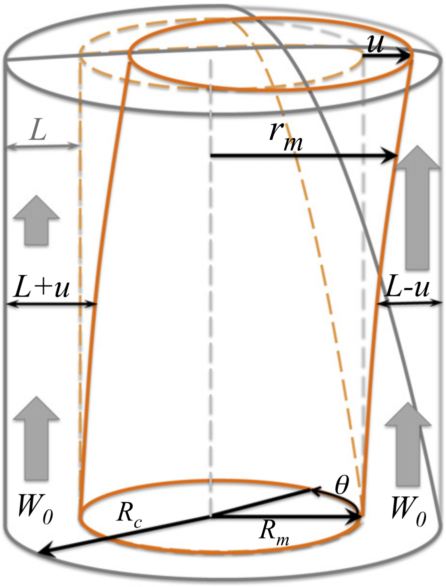

Fig. 1. Sketch of the cylindrical annulus for the magma-wagging model proposed by Bercovici et al. (2013). The displacement $\vec{u}$ is always oriented in the same plane for different time and vertical position.

2. Evolution of magma motion in three dimensions

The motion of a magma column with an angular component can be presented by a 2-D displacement vector $\vec{u} = \vec{u}(z,t)$ at time t and height z along the column (see Fig. 2a). In polar coordinates, $\vec{u}$ is expressed by its magnitude $u(z,t)$ and its polar angle $\phi(z,t)$, measured relative to the direction $\hat{x}$ (see Fig. 2b). Once $\hat{x}$ is arbitrarily selected, it remains the same for the whole magma column at all times. (Equivalently, $\vec{u}$ can be described in Cartesian coordinate with the bases $\hat{x}$ and $\hat{y}$ in which $\hat{x}$ is aligned with the direction of $\phi = 0$.) We next define an arbitrary point Q on the surface of the magma column with a polar angle θ (see Fig. 2). Q's position $\vec{r}_m$ satisfies

$$\begin{aligned} R_m^2 &= \left|\vec{r}_m - \vec{u}\right|^2 \\ &= (r_m \cos\theta - u\cos\phi)^2 + (r_m \sin\theta - u\sin\phi)^2 \\ &= r_m^2 - 2r_m u\cos(\theta-\phi) + u^2 \end{aligned} \tag{2}$$

The displacement of the magma column is very small compared to the outer conduit radius, and thus $u \le R_c - R_m << R_m$. To first order in u, Eq. (2) yields

$$r_m = R_m + u\cos(\theta - \phi) \tag{3}$$

For a simple foam model (where there is no gas flux through the annulus), we want to infer how much the annulus is compressed or dilated by the column displacement, and thus how the gas pressure

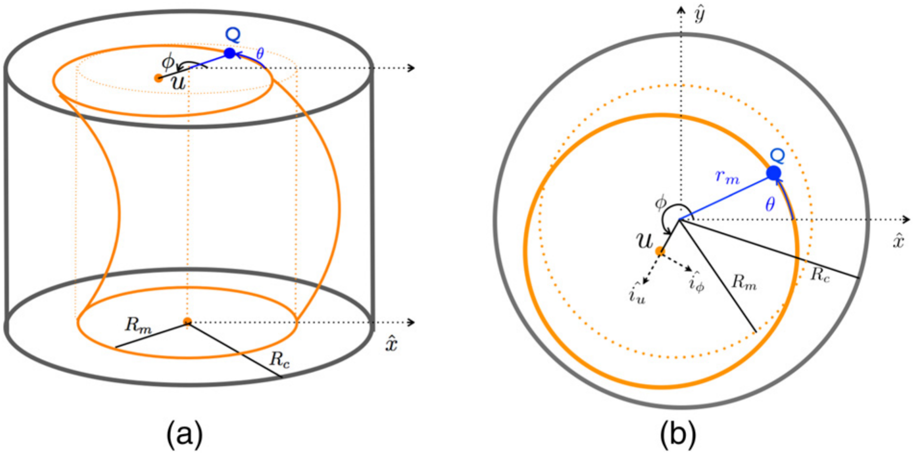

Fig. 2. (a) Sketch of the magma column in the three-dimensional wagging model. ϕ is the polar angle of the magma column's displacement, u is the radius displacement, or equivalently the displacement magnitude. R_c and R_m are the radii of the magma column and volcanic conduit, respectively. (b) Top view of an intersection of the magma column. The dashed lines denote the unit vectors of either the Cartesian system $\hat{x}$ and $\hat{y}$, or the cylindrical-polar system $\hat{\imath}_u$ and $\hat{\imath}_\phi$. Q is any arbitrary point on the surface of the magma column.

responds. Measured from $Q(r_m, \theta)$, the volume of the annulus segment spanned by angular increment $d\theta$ and vertical increment dz is

$$dV = dz\int_{r_m}^{R_c} \mathrm{r}\mathrm{d}\theta\mathrm{d}\mathrm{r} = dV_o\left[1-\frac{u}{U}\cos\left(\theta-\phi\right)\right] \tag{4}$$

where $U \equiv \left(R_c^2 - R_m^2\right)/2R_m$, and the undisturbed volume of the annulus section is $dV_o = \frac{1}{2}\left(R_c^2 - R_m^2\right) d\theta dz$. We let Φ_o be the gas volume fraction in the undisturbed annulus, and assume that the magma volume in the same section $dV_m = dV_o(1 - \Phi_o)$ is conserved; in this case, the gas volume in the same section of the deformed annulus becomes

$$dV_g = dV - dV_m = dV_o\left[\Phi_o - \frac{u}{U}\cos\left(\theta-\phi\right)\right] \tag{5}$$

Assuming that the annulus contains disconnected bubbles filled with ideal gas, then the gas pressure obeys

$$P = \frac{RT\frac{dM_g}{m_g}}{dV_g} = \rho_o C_g^2 \frac{1}{1-\frac{u\cos(\theta-\phi)}{U\Phi_o}} \tag{6}$$

where R is the gas constant, T is the temperature, m_g is the molecular mass of the gas, C_g is the isothermal gas sound speed at temperature T, $dM_g = \rho_o\Phi_o dV_o$ is the gas mass in the segment, and ρ_o is the undisturbed gas density. For small displacement such that $u \ll U$, Eq. (6) is to first order

$$P(\theta) = \rho_o C_g^2\left(1 + \frac{u\cos\left(\theta-\phi\right)}{U\Phi_o}\right) \tag{7}$$

Therefore, the traction (force per area) $\mathcal{T}$ due to the gas pressure acting on the magma column at point Q and parallel to the displacement is

$$\mathcal{T} = -P\frac{\left(\vec{r}_m - \vec{u}\right).\vec{u}}{\left|\vec{r}_m - \vec{u}\right|u} = -\rho_o C_g^2\left(1 + \frac{u\cos\left(\theta-\phi\right)}{U\Phi_o}\right) \times\left[\cos\left(\theta-\phi\right) - \frac{u}{R_m}\sin^2\left(\theta-\phi\right)\right] \tag{8}$$

The net pressure force $\vec{F}_p$ acting on the whole magma column section is

$$\vec{F}_p = dz\int_{\phi-\pi}^{\phi+\pi}\mathcal{T}r_m\mathrm{d}\theta\hat{\mathrm{u}} = -dz\rho_o C_g^2\frac{\pi R_m\vec{u}}{U\Phi_o} = -\omega_o^2\,\vec{u}\,dm \tag{9}$$

where the mass of the magma column section is $dm = dz\rho_m\pi R_m^2$ for given magma density ρ_m, $\hat{\mathrm{u}}$ is the unit vector in the direction of $\vec{u}$, and ω_o is given by Eq. (1). In addition to the pressure force, a resistance force $\vec{F}_s$ acts against the bending of the magma column section. $\vec{F}_s$ results from the difference in the shear traction on the upper and lower surfaces of a horizontal segment of the magma column of thickness dz and mass dm. The magma is assumed to behave like a viscous Newtonian fluid with uniform dynamic viscosity μ_m. For any horizontal intersection of the magma column, the whole area moves with uniform velocity $\partial\vec{u}/\partial t$ (again assuming small displacement). The traction vector due to shear stress tensor $\boldsymbol{\tau}$ acting at the top or bottom of the segment

$$\boldsymbol{\tau}.\hat{z} = \mu_m\frac{\partial}{\partial z}\frac{\partial\vec{u}}{\partial t} \tag{10}$$

has non-vanishing components τ_{uz} and $\tau_{\theta z}$. The total force $\vec{F}_s$ is from the difference in tractions across the section's lower and upper surfaces

$$\vec{F}_s = [\boldsymbol{\tau}]|_z^{z+dz}\,\pi R_m^2 = \mu_m\pi R_m^2 dz\frac{\partial^2}{\partial z^2}\frac{\partial\vec{u}}{\partial t} \tag{11}$$

where πR_m^2 is the cross-section area of the column section. Newton's second law for the magma column section with mass dm becomes

$$dm\frac{\partial^2\vec{u}}{\partial t^2} = \vec{F}_p + \vec{F}_s \tag{12}$$

which leads to

$$\frac{\partial^2\vec{u}}{\partial t^2} = -\omega_o^2\vec{u} + \nu_m\frac{\partial^2}{\partial z^2}\frac{\partial\vec{u}}{\partial t} \tag{13}$$

where $\nu_m = \mu_m/\rho_m$ is the kinematic viscosity. Note that ω_o is the frequency of free-oscillation, and has the same value as the fundamental frequency in the 2-D wagging model with the same conduit properties (Bercovici et al., 2013; Jellinek and Bercovici, 2011).

3. Free whirling motions

As shown by Jellinek and Bercovici (2011), the magma column viscosity controls the damping of the wagging motion (over a damping time scale $\tau_s \sim \nu_m^{-1}k^{-2}$), but has a minor influence on its oscillation frequency, which is associated with the gas spring force. Therefore, to better understand the magma-annulus interaction, we first consider a system with very long vertical wavelength, i.e., $k \to 0$, in which case viscous damping becomes negligible, and the system approaches an inviscid limit. Under the long-wavelength assumption, displacement is continuous with a small vertical gradient along the z direction. At an arbitrary height, the horizontal section of the magma column orbits around the center of the conduit, and the whirling motion can be represented as a trajectory by $u = u(t), \phi = \phi(t)$. Without the viscous term, the equation of motion Eq. (13) becomes

$$\frac{\partial^2 \vec{u}}{\partial t^2} = -\omega_o^2 \vec{u} \tag{14}$$

In cylindrical-polar coordinate, Eq. (14) is expressed as two evolution equations, in radial direction and tangential direction, respectively (Batchelor, 1967):

$$\frac{d^2u}{dt^2} - u\frac{d\phi}{dt}\frac{d\phi}{dt} + \omega_o^2 u = 0 \tag{15}$$

$$u\frac{d^2\phi}{dt^2} + 2\frac{du}{dt}\frac{d\phi}{dt} = 0 \tag{16}$$

where u and ϕ are the magnitude of displacement and the polar angle of the displacement, respectively (see Fig. 2b). We define the specific angular momentum (angular momentum per unit mass) $L \equiv u^2(d\phi/dt)$ and specific energy (energy per unit mass) $E \equiv \frac{1}{2}\left(\frac{du}{dt}\right)^2 + \frac{1}{2}u^2\left(\frac{d\phi}{dt}\right)^2 + \frac{1}{2}\omega_o^2 u^2$, respectively. Eq. (16) shows that $dL/dt = 0$, and both Eqs. (15) and (16) together show that $dE/dt = 0$. The trajectory therefore can be expressed as conservation of total energy (kinetic and potential) and angular momentum

$$E_o = \frac{1}{2}\left(\frac{du(t)}{dt}\right)^2 + \frac{1}{2}u(t)^2\left(\frac{d\phi(t)}{dt}\right)^2 + \frac{1}{2}\omega_o^2 u(t)^2 \tag{17a}$$

$$L_o = u(t)^2\frac{d\phi(t)}{dt} \tag{17b}$$

Once the energy and angular momentum of the system are determined by the initial conditions, a steady state circular solution, or 'whirling' motion, can be found immediately by letting $du/dt = 0$. This solution corresponds to a circular orbit with constant radius and angular velocity

$$u_o = \sqrt{\frac{L_o}{\omega_o}}, \quad \text{and} \quad \frac{d\phi}{dt} = \omega_o, \tag{18}$$

respectively, whose period is $T_o = 2\pi/\omega_o$. Other solutions to Eq. (15)–(17) correspond to different sets of closed elliptical trajectories given by (see Appendix A)

$$\pm\cos 2\phi = \frac{\mathcal{E} - \frac{L_o}{\omega_o u^2}}{\sqrt{\mathcal{E}^2 - 1}} \tag{19}$$

where the dimensionless number $\mathcal{E} \equiv E_o/L_o\omega_o \geq 1$. When $\mathcal{E} = 1$, the circular solution is recovered, and the system has the lowest energy for a given angular momentum. Both Eqs. (19) and (17) yield

$$\frac{d\phi}{dt} = \omega_o\left(\mathcal{E} - \sqrt{\mathcal{E}^2 - 1}\cos 2\phi\right) \tag{20}$$

The period of the trajectory, corresponding to an increment in ϕ of 2π, can be found from Eq. (20) (see Appendix A), which yields $T_o = 2\pi/\omega_o$, same as the period for the circular whirling solution. Note that the trajectory described by Eq. (19) can also be expressed as the classical equation for an ellipse (see Appendix A)

$$\frac{x^2}{a^2} + \frac{y^2}{b^2} = 1 \tag{21}$$

where $x = u\cos\phi, y = u\sin\phi$, and a and b are the lengths of the major and minor axis of the ellipse: the relation of Eqs. (21) to (19) yields

$$\begin{aligned} a^2 &= \frac{L_o}{\omega_o}\frac{1}{\mathcal{E} - \sqrt{\mathcal{E}^2 - 1}} \\ b^2 &= \frac{L_o}{\omega_o}\frac{1}{\mathcal{E} + \sqrt{\mathcal{E}^2 - 1}} \end{aligned} \tag{22}$$

The eccentricity of the elliptical whirling orbit in Eq. (21) is $e \equiv \sqrt{1 - b^2/a^2}$, or

$$e = \sqrt{1 - \frac{\mathcal{E} - \sqrt{\mathcal{E}^2 - 1}}{\mathcal{E} + \sqrt{\mathcal{E}^2 - 1}}} \tag{23}$$

For a specific angular momentum, an increase in energy E (or equivalently $\mathcal{E}$) causes more elliptical orbits (see Fig. 3). At very high energy, the whirling orbit has eccentricity close to 1, which corresponds to the 2-D 'side-to-side' wagging in a single plane. The 2-D magma wagging motion studied by Jellinek and Bercovici (2011) and Bercovici et al. (2013) is therefore a subset of the whirling orbits.

4. Numerical analysis of damped oscillations

When the effect of viscous damping is included, the free oscillations of the magma column are damped by viscous resistance in the absence of a driving mechanism. The viscous force, according to Eq. (11), is influenced by the non-uniform displacement of the magma column in both radial, as well as angular directions. The shapes of the displaced magma column can be categorized into two classes: coiled shape and uncoiled shape. For the uncoiled magma column (see Fig. 5a), the polar angle ϕ is the same and changes at

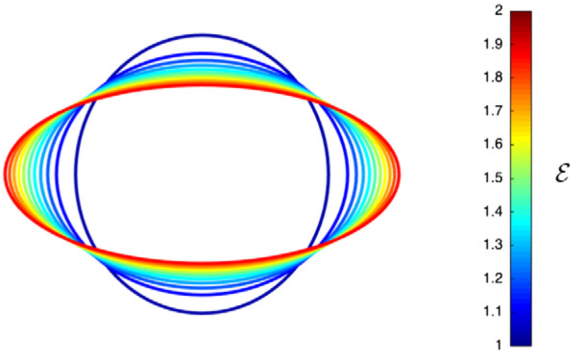

Fig. 3. Colored solid lines are different elliptical whirling orbits corresponding to different $\mathcal{E} = E_o/L_o\omega_o$ ranging from 1 to 2. Colorbar indicates the values of $\mathcal{E}$. The trajectory is more elliptical when energy E_o (or equivalently $\mathcal{E}$) increases.

the same rate for all z; for the coiled magma column, ϕ may have different values, or change at different rates along the column (see Fig. 5e). Under specific radial displacement, the coiled magma column bends more than the uncoiled column, and thus is subjected to stronger viscous damping. In this scenario, the evolution of the coiled magma column is poorly approximated by the inviscid solution, as its strong bending violates the long vertical-wavelength assumption for the inviscid approximation. The viscous governing Eq. (13) can be written in Cartesian coordinates as

$$\frac{\partial^2 x}{\partial t^2} + \omega_o^2 x = \nu_m \frac{\partial^3 x}{\partial z^2 \partial t} \tag{24a}$$

$$\frac{\partial^2 y}{\partial t^2} + \omega_o^2 y = \nu_m \frac{\partial^3 y}{\partial z^2 \partial t} \tag{24b}$$

where x and y are the two components of the displacement vector $\vec{u}$. The solution of both Eq. (24a) and (24b) can be expressed as a superposition of Fourier modes with vertical wave-numbers k_x and k_y, respectively (see Fig. 4).

At moderately long wavelengths ($k_j < \sqrt{2\omega_o/\nu_m}$, $j = x$ or y), the modes obey the damping functions $\exp\left(-\nu_m k_x^2 t/2\right)$ for x and $\exp\left(-\nu_m k_y^2 t/2\right)$ for y, which are identical in form to that of the 2-D wagging model (Jellinek and Bercovici, 2011). In three dimensions, the displacement magnitude $u = \sqrt{x^2 + y^2}$ is a nonlinear combination of the two solutions. We solve Eq.(24) numerically with finite difference and semi-implicit time-stepping using a tridiagonal matrix algorithm, and explore the behavior of the magma column, subjected to both pressure and viscous forces, for both classes of shapes as initial conditions. We consider the base of the magma column $z = 0$ to be at the depth where gas exsolution is insufficient to form an annulus enveloping the magma column. Below this depth, the column is confined directly by the conduit with no displacement, thus $u|_{z=0} = 0$. We also assume a free surface at the top of the column $z = H$, where $\partial u/\partial z|_{z=H} = 0$. These boundary conditions determine that the longest wave-length in the displacement permitted for the magma column is $4H$, where H is the height of the magma column. Jellinek and Bercovici (2011) show that the perturbation with the longest possible wavelength damps more slowly than other wavelengths and therefore lasts longer. To study the long-term damping behavior, we let the initial displacement magnitude $u|_{t=0} \sim sin(2\pi z/4H)$ for both coiled and uncoiled cases. For the uncoiled case, the initial angular displacement $\phi|_{t=0} = 0$ and angular velocity $\frac{\partial\phi}{\partial t}|_{t=0} = \omega_o$ are both independent of z; for the coiled case, the initial angular displacement varies along z according to $\phi|_{t=0} = 4\pi z/H$, giving the column a coiled shape.

4.1. Damping of uncoiled magma column

When the magma column is uncoiled, the initial angular displacement ϕ and angular velocity $\partial\phi/\partial t$ are the same for all values of z (see Fig. 5a). With uncoiled initial conditions, the magma column remains uncoiled at all times, and the radial displacement u decreases according to the same decay function $exp(-\nu_m k^2 t/2)$ predicted in the 2-D model (Jellinek and Bercovici, 2011) (see Fig. 5b). As discussed in § 3, the magma column whirls along closed elliptical orbit when the viscous effect is absent. When the viscous force damps the motion of the uncoiled magma column, the elliptical orbit shrinks and collapses but the shape (eccentricity) of the orbit remains (Fig. 5d).

4.2. Coiled magma column

When the magma column is coiled, the polar angle ϕ and the angular velocity $\partial\phi/\partial t$ are non-uniform along z (Fig. 5e). The non-vanishing contributions of $\partial\phi/\partial z$ and $\partial(\partial\phi/\partial t)/\partial z$ cause stronger deformation and induce extra viscous resistance. Compared with the uncoiled case discussed previously, wherein u decays identically as for 2-D wagging (Fig. 5b), the coiled magma column has a higher decay rate (see Fig. 5f). The coiling of the magma column introduces smaller wavelengths in both x and y, which result in oscillations with lower frequencies (Fig. 5g) and faster viscous damping (Fig. 5f)

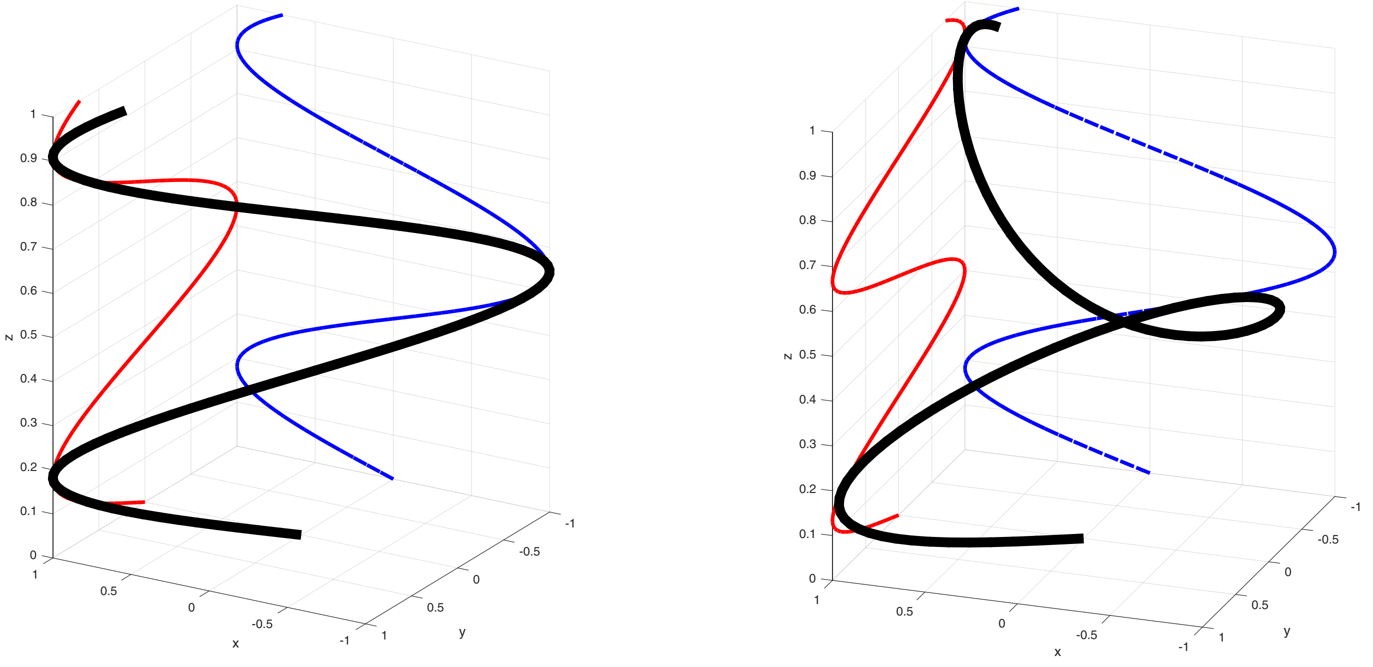

(a)

(b)

Fig. 4. 3D shape (black line) defined by vertical wave-numbers k_x and k_y. In panel (a) $k_x = k_y = 11\pi/4$; in panel (b), $k_x = 11\pi/4$ and $k_y = 15\pi/4$. Variation of x and y along z axis are shown in blue and red, respectively.

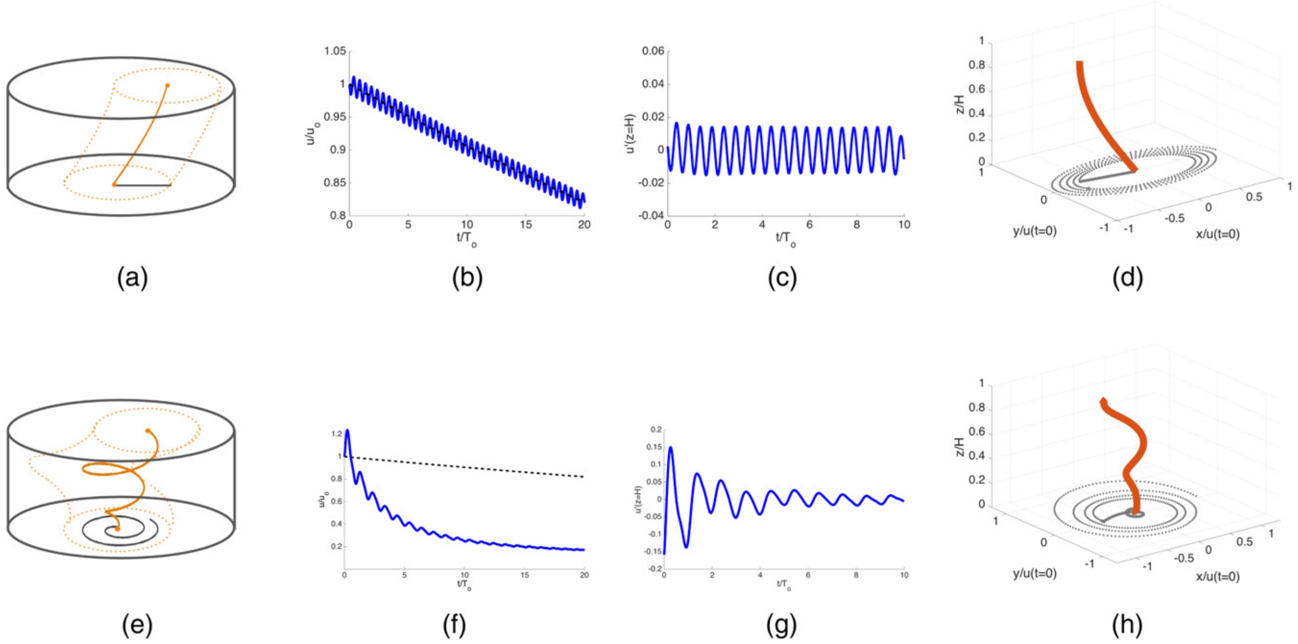

Fig. 5. Examples of uncoiled (top row) and coiled (bottom row) magma column whirling with viscous damping. The magnitudes of the initial displacement for both cases are $u(t=0,z) \sim sin(\pi z/2H)$, where H is the total height of the magma column, and the initial angular velocity $d\phi/dt(t=0,z)=\omega_o$. The initial angular displacement for the uncoiled magma column is $\phi(t=0,z)=0$, and for the coiled magma column $\phi(t=0,z)=4\pi z/H$. Frames (a) and (e) show the initial displacement of the magma column (orange) in three dimensions, with their 2-D projections on the horizontal plane (gray). Frames (b) and (f) show the change of radial displacement u at the top of the magma column; the black dashed line indicates the decay function predicted for the 2-D model $exp(-\nu_m(\pi/2H)^2t/2)$. Frames (c) and (g) show the evolution of u calculated from the curves in (b) and (f) but subtracting the decay trend. Frames (d) and (h) show the instantaneous displacements of the magma columns during damping; trajectories of the top of the magma column are shown in gray dots.

(Jellinek and Bercovici, 2011). As a result, the coiled magma column tends to be smoothed by the extra viscous dissipation rapidly (Fig. 5h), and results in long-lasting uncoiled wagging.

5. Seismic signature of magma wagging

5.1. Propagation of seismic waves generated by whirling motions

The eccentricity of the elliptical whirling orbit is determined by the magma column's energy and angular momentum (see Eq. (23)), which may undergo significant change before an eruption. Other characteristics of the wagging motion, such as the direction of the whirling and the orientation of the elliptical orbit could also change when an eruption is approaching. These predictions can be tested if the wagging motion is detectable using field measurements. Here, we seek to understand how the wagging motion induces a seismic signal in the crustal medium around the volcanic conduit, so that we can detect the wagging characteristics with field data, and test our model with seismic observations as well.

For simplicity, we assume the volcanic conduit is surrounded by a homogenous, isotropic medium that responds elastically to the change of pressure in the conduit due to the wagging magma column. Consequently, as the magma column wags inside the gas-rich annulus, resulting pressure variations on the inner conduit wall are transmitted to the medium outside the conduit as seismic compressional or P-waves, which in principle can be detected by seismometers placed around the volcano. Here, we analyze the P-waves generated by inviscid free wagging (i.e., assuming there is a forcing or excitation mechanism to offset viscous damping; see Bercovici et al. (2013)). We assume that the displacement of the magma column involves the longest wavelength (e.g., $\lambda_{\max}=4H$, where H is the height of the magma column, and assuming a free-slip surface at the vent; see (Jellinek and Bercovici, 2011)) and an 'un-coiled' shape, which is the least damped oscillatory mode; this leads to negligible vertical normal strain in the elastic media surrounding the conduit, hence P-waves are predominantly two-dimensional. The medium around the volcanic conduit has a displacement field $\vec{U}(r,\theta,t)$ where r and θ are radial distance and polar angle measured from the center of the conduit. The pressure Π in the medium is defined by the volumetric dilation $\Pi \equiv -\kappa\nabla.\vec{U}$, where κ is the bulk modulus of the medium. Π satisfies the compressional wave equation

$$\frac{\partial^2\Pi}{\partial t^2}-c^2\nabla^2\Pi=0 \qquad (25)$$

where c is the P-wave velocity in the surrounding medium. The mechanical pressure acting on the conduit wall by the annulus, given by Eq. (7), has a static value $P_o=P(u=0)=\rho_o C_g^2$. During magma wagging, the increment in pressure $\Delta P=P-P_o=\rho_o C_g^2 u\cos(\theta-\phi)/U\Phi_o$ is balanced by the deformation of the surrounding rock, which leads to an inner boundary condition for Eq. (25) at $r=R_c$

$$\Pi(R_c,\theta,t)=\Delta P \qquad (26)$$

Pressure perturbations are then caused by free wagging motion described by the elliptical orbit (21). With the initial condition $x(t=0)=a, dx/dt(t=0)=0$ and counter-clockwise whirling motion, the solution of the trajectory is $x=u\mathrm{cos}\phi=a\mathrm{cos}(\omega_o t), y=u\mathrm{sin}\phi=b\mathrm{sin}(\omega_o t)$, which yields another expression of the inner boundary condition

$$\Pi(R_c,\theta,t)=\frac{a\rho_o C_g^2}{U\Phi_o}\cos(\omega_o t)\cos\theta+\frac{b\rho_o C_g^2}{U\Phi_o}\sin(\omega_o t)\sin\theta \qquad (27)$$

Away from the conduit, we assume an infinite domain in the radial direction. Except for the conduit wall, there is no other solid boundary, so the P-waves only travel radially outward from the conduit without reflection. With these boundary conditions, P-waves obey the solution (see Appendix B.1)

$$\begin{aligned}\Pi(r,\theta,t) = &\cos(\omega_o t)\cos\theta\left(a_1 J_1\left(\frac{\omega_o}{c}r\right) - b_1 Y_1\left(\frac{\omega_o}{c}r\right)\right)\\ &+\sin(\omega_o t)\sin\theta\left(c_1 Y_1\left(\frac{\omega_o}{c}r\right) + d_1 J_1\left(\frac{\omega_o}{c}r\right)\right)\\ &+\sin(\omega_o t)\cos\theta\left(a_1 Y_1\left(\frac{\omega_o}{c}r\right) + b_1 J_1\left(\frac{\omega_o}{c}r\right)\right)\\ &+\cos(\omega_o t)\sin\theta\left(c_1 J_1\left(\frac{\omega_o}{c}r\right) - d_1 Y_1\left(\frac{\omega_o}{c}r\right)\right)\end{aligned} \tag{28}$$

where

$$(a_1,b_1,c_1,d_1) = K*\left(aJ_1\left(\frac{\omega_o}{c}R_c\right), -aY_1\left(\frac{\omega_o}{c}R_c\right), bY_1\left(\frac{\omega_o}{c}R_c\right), bJ_1\left(\frac{\omega_o}{c}R_c\right)\right) \tag{29}$$

in which $K = \rho_o C_g^2 / U\Phi_o \left(J_1(\omega_o R_c/c)^2 + Y_1(\omega_o R_c/c)^2\right)$, and a and b are the lengths of the major and minor axis of the elliptical trajectory, respectively. Solution (28) corresponds to a counter-clockwise elliptical wagging orbit with the major axis along the $\hat{x}$ direction. When the major axis is tilted at an angle $\delta\theta$ or the wagging direction is clockwise, the P-wave solution can be obtained by performing the transform $\theta \to \theta - \delta\theta$ and $\theta \to -\theta$, respectively (see Appendix B.1).

The P-wave radiation patterns given by Π are diagnostic of the three different wagging orbits, calculated by Eqs. (28) and (29) (see Fig. 6). Specifically, the 2-D wagging orbit (similar to that of Jellinek and Bercovici (2011) and Bercovici et al. (2013)) generates dipolar radiation pattern, with perfect mirror symmetry about the direction of wagging (see Fig. 6a). The elliptical wagging orbit generates closed, disconnected patches of high-and-low pressure spiraling outward (see Fig. 6c). At a position (r,θ) outside the conduit (see Fig. 14 in Appendix B.1), the measured P-wave can be expressed as a time series in Π:

$$\Pi(r,\theta,t) = \Pi_{\max}\cos(\omega_o t - \psi_r - \psi_\theta) \tag{30}$$

where the maximum pressure $\Pi_{\max}$, and the phase-shifts in radial distance ψ_r and in polar angle ψ_θ are defined as

$$\begin{aligned}\Pi_{\max}(r,\theta) =&\frac{\rho_o C_g^2}{U\Phi_o}\sqrt{\frac{J_1\left(\frac{\omega_o}{c}r\right)^2 + Y_1\left(\frac{\omega_o}{c}r\right)^2}{J_1\left(\frac{\omega_o}{c}R_c\right)^2 + Y_1\left(\frac{\omega_o}{c}R_c\right)^2}}\sqrt{a^2\cos^2\theta + b^2\sin^2\theta}\\ \psi_r(r) =&\tan^{-1}\left(\frac{J_1\left(\frac{\omega_o}{c}R_c\right)Y_1\left(\frac{\omega_o}{c}r\right) - Y_1\left(\frac{\omega_o}{c}R_c\right)J_1\left(\frac{\omega_o}{c}r\right)}{J_1\left(\frac{\omega_o}{c}R_c\right)J_1\left(\frac{\omega_o}{c}r\right) + Y_1\left(\frac{\omega_o}{c}R_c\right)Y_1\left(\frac{\omega_o}{c}r\right)}\right)\\ \psi_\theta(\theta) =&\tan^{-1}\left(\frac{\pm b\sin(\theta-\delta\theta)}{a\cos(\theta-\delta\theta)}\right).\end{aligned} \tag{31}$$

Here, ± indicates counter-clockwise (+), and clockwise (−) whirling, and $\delta\theta$ is the angle between the direction of the major axis of the elliptical trajectory and $\hat{x}$ direction (see Fig. 14 in Appendix B.1). As the magma column whirls, the induced P-waves consist of monochromatic oscillations described by Eq. (30), and the comparisons between P-waves at different locations can be used to deduce the characteristics of the wagging motion. If the P-waves are recorded at the same radial distance from the conduit but at different polar angles, and the signals are completely in-phase (when the peaks arrive at the same time) or completely out-of-phase (when the peaks are offset by half period in time), then 2-D side-to-side wagging is indicated, since $\psi_\theta = 0$ when $b = 0$. If the signals share the same maximum amplitude but are offset by a measurable phase-lag, then circular wagging is indicated as $\Pi_{\max} = \Pi_{\max}(r)$ when $b = a$. If the signals are different in both their amplitudes and phases, then elliptical wagging orbit is indicated.

5.2. Wagging signal diagnostics

In this section, we outline a method to identify the wagging signal in seismic data. The approach is based on calculating the relative time-lag between seismic station pairs, which is a quantity obtained by calculating pairwise cross-correlation functions of the seismic waveforms. Specifically, when a pair of seismic stations A and B share the same radial distance $r^{(A)} = r^{(B)}$ but have different angles $\theta^{(A)}$ and $\theta^{(B)}$, the time-lag between their waveforms becomes $\text{Lag}_{A-B} = \left(\psi_\theta^{(B)} - \psi_\theta^{(A)}\right)/\omega_o$, in which $\psi_\theta^{(A)}$ and $\psi_\theta^{(B)}$ are values of ψ_θ evaluated at station A and B according to Eq. (31). $\text{Lag}_{A\text{-}B}$ has the unit of time, and is further related to the spatial properties of the wagging pattern. The time-lag also indicates how long it takes the magma column to move from one maximally compressed part of the annulus to another. For example, for two-dimensional wagging, half of the annulus is compressed at the same time, leading to waveforms on that side of the annulus (i.e., detected by seismometers on that side) that are in-phase with each other, with zero time-lag. The other half of the annulus is compressed after the magma column leans to its side after half period; this leads to waveforms that have a half-period time-lag relative to those on the opposite (now dilated) side. For three-dimensional circular whirling, the lag between any two stations would be the time interval between closest approach of the whirling column as it swings from one station to the next. Below we describe the basic features of P-wave cross-correlations predicted for two-dimensional wagging and three-dimensional wagging, respectively.

5.2.1. Side-to-side wagging

When the magma column undergoes 2-D wagging, the length of the minor axis $b = 0$. The seismic radiation pattern (see Fig. 6a) is symmetric with respect to the wagging direction. Using $b = 0$ in Eqs. (30) and (31), the phase-shift $\psi_\theta(\theta)$ only has two possible values: $\psi_\theta(\theta) = 0$ when $|\theta - \delta\theta| < \pi/2$, or $\psi_\theta(\theta) = \pi$ when $|\theta - \delta\theta| >$

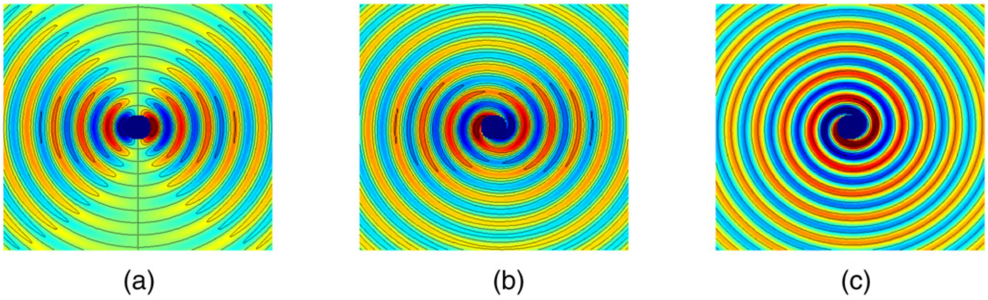

Fig. 6. Examples of P-waves radiation patterns (instantaneous values of pressure) generated by magma wagging with displacement trajectories corresponding to (a) 2-D side-to-side wagging with eccentricity $e = 1$; (b) counter-clockwise elliptical whirling motion with eccentricity $e = 0.8$; and (c) counter-clockwise circular whirling with $e = 0$. The colormap shows the values of Π calculated according to Eqs. (28) and (29).

$\pi/2$. For locations with $|\theta - \delta\theta| = \pi/2$, the P-waves vanish. For any given seismic stations A (located at $(r^{(A)}, \theta^{(A)})$), and B (located at $(r^{(B)}, \theta^{(B)})$), a station pair A-B is formed with a time-lag between the waveforms $\text{Lag}_{A\text{-}B}$ (e.g. $\text{Lag}_{E\text{-}S}$ of station pair E-S formed by east station E and south station S in Fig. 7). When A and B share the same radial distance $r^{(A)} = r^{(B)}$ (see Fig. 7a), the time-lag between the two stations becomes $\text{Lag}_{A-B} = \left(\psi_\theta^{(B)} - \psi_\theta^{(A)}\right)/\omega_o$, and has two possible values: $\text{Lag}_{A\text{-}B} = 0$ when A and B both occur in the half plane divided by $|\theta - \delta\theta| = \pi/2$ (e.g. station pairs N-E, S-W, N-NE in Fig. 7a), or $\text{Lag}_{A\text{-}B} = T_o/2$ when A and B are in different half planes (e.g. station pairs N-S, N-W, NE-S in Fig. 7a). In the former case, the waveforms recorded by the two stations are completely in-phase; in the later case, the waveforms are completely out-of-phase (see Fig. 7c). Note that for a pair of seismic stations that are located with 180 ° apart with $\theta^{(A)} = \pi + \theta^{(B)}$, the time-lags always satisfy $\text{Lag}_{A\text{-}B} = T_o/2$ for both two-dimensional and three-dimensional wagging, with the only exception of vanishing waveforms. Therefore, the time-lag between stations with 180° separation is insensitive to the wagging pattern, and we choose stations with 90° separation to diagnose different wagging patterns here.

5.2.2. Three-dimensional wagging

When the magma column undergoes three-dimensional wagging described by an elliptical whirling orbit with non-vanishing minor axis $b \neq 0$, the P-waves measured at different locations can have different phase-shifts. The waveforms generated by three-dimensional wagging (Fig. 8c), unlike those generated by the 2-D wagging (Fig. 7c), can be neither completely in-phase nor out-of-phase with each other. As a result, the time-lags between the seismic station pairs (see Fig. 8b) can range from 0 to one wagging period T_o.

For any pair of seismic stations with 90° separation and the same distance to the conduit, the time-lag between the stations is a function of the wagging orientation ($\delta\theta$), direction (clockwise or counter-clockwise) and eccentricity e (see Fig. 9). For two specific stations (such as station E and station S shown in Fig. 8a), the possible value of the time-lag between them always falls within two envelopes (see Fig. 9) defined by (see Appendix B.2)

$$\text{Lag}_{E-S}/T_o = \begin{cases} \frac{1}{2} + \frac{1}{\pi}\tan^{-1}((1-e^2)^{\pm 1/2}), & \text{for clockwise motion} \\ \frac{1}{2} - \frac{1}{\pi}\tan^{-1}((1-e^2)^{\pm 1/2}), & \text{for counter-clockwise motion} \end{cases} \tag{32}$$

As the time-lag only exists within these two envelopes, the observed time-lag provides constraints on the possible values of eccentricity, as well as wagging orientation. For example, if $\text{Lag}_{E\text{-}S} = 0.9T_o$, the envelopes require clockwise wagging with northwest-southeast orientation of the major elliptical axis (see Fig. 9 and Appendix B.2 Table 1), and eccentricity confined between 0.9 and 1; if $\text{Lag}_{E\text{-}S} = 0.4T_o$, then the wagging is counter-clockwise with northeast-southwest orientation, and eccentricity between 0.95 and 1. When $\text{Lag}_{E\text{-}S} = T_o/4$ or $3T_o/4$, all values of eccentricity are possible but only when the wagging orientation is either in the north-south or east-west direction (i.e., $\delta\theta = 0°$ or $90°$). However, if the time-lag

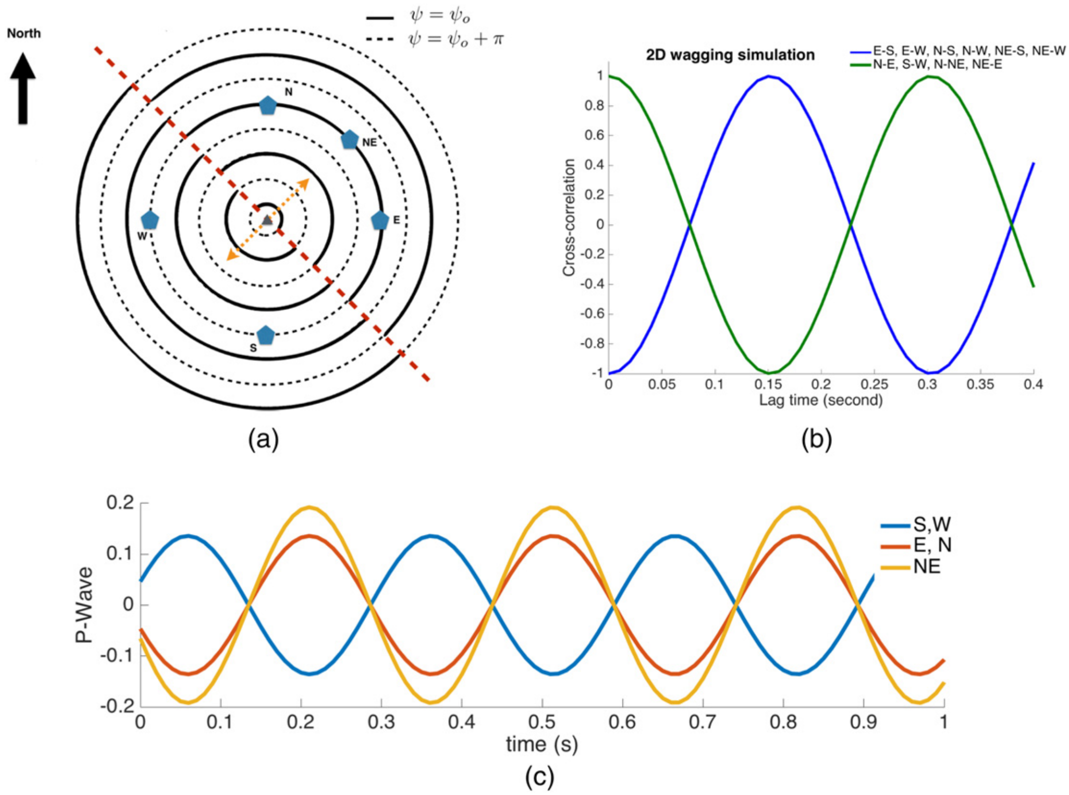

Fig. 7. (a) Contours of phase-shift of P-waves generated by 2-D wagging at frequency of 3.3 HZ. Black solid lines and dash lines are two groups of equal-phase contours which are out-of-phase with each other (the maximum value of one group of contours corresponds to minimum value of the other in time). The gray triangle in the center of the contours indicates the location of the conduit. Pentagons indicate the locations of five virtual seismic stations located at the north (station N), east (station E), south (station S), west (station W) and northeast (station NE) of the conduit with equal distance of 2 km. The orange dash line with arrowhead indicates the direction of the wagging plane, which is northeast-southwest direction with $\delta\theta = 45°$. The contours indicate that any two stations located at the same distance to the conduit are either in-phase (when located in the same side of the red dash line), or out-of-phase with each other (when located in the opposite sides of the red dash line). (c) P-waves calculated at the five virtual stations shown in (a), which are in-phase or out-of-phase with the others. (b) Cross-correlation functions of P-waves for different station pairs. The blue curve is the cross correlation between stations that are out-of-phase with each other; the green curve is the cross correlation between stations that are in-phase with each other. Station pairs that are in-phase have maximum cross-correlation at 0; stations which are out-of-phase have maximum cross-correlation at $T_o/2 = 0.15$ s.

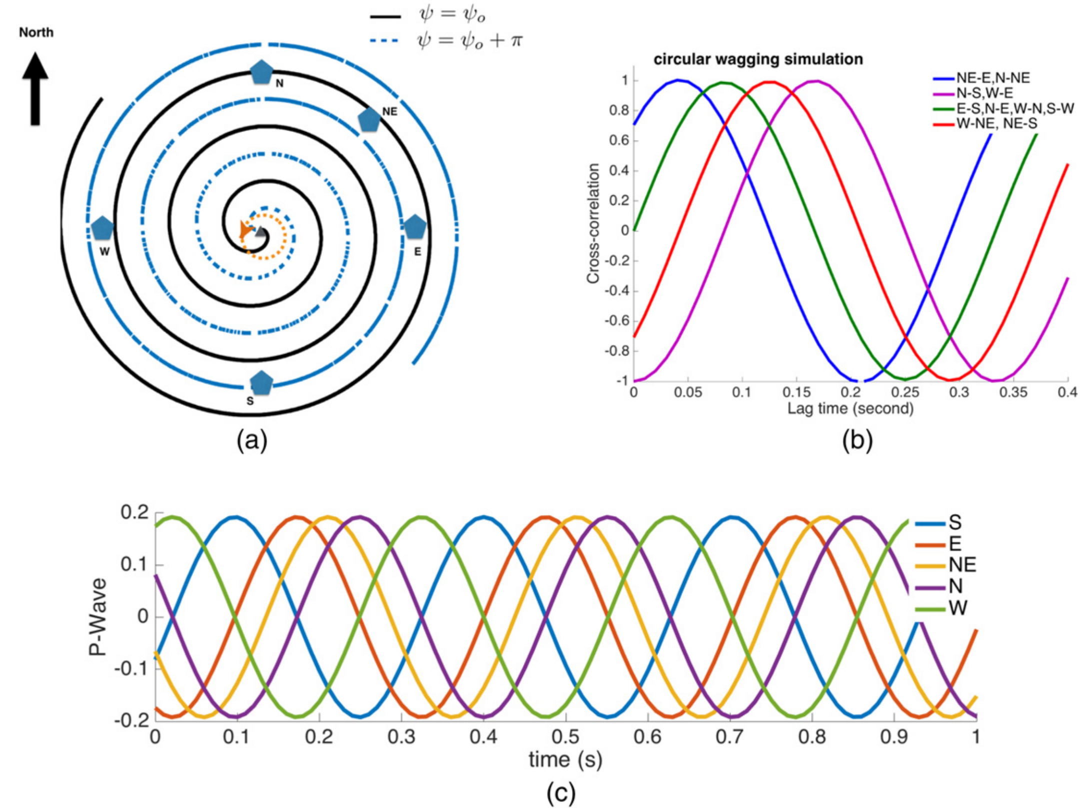

Fig. 8. (a) Contours of phase-shift of P-waves generated by a counter-clockwise wagging with circular whirling orbit at frequency of 3.3 HZ. Black solid lines and blue dash lines are two groups of equal-phase contours that are out-of-phase with each other. Pentagons indicate the locations of five virtual seismic stations located at the north (station N), east (station E), south (station S), west (station W) and northeast (station NE) of the conduit (gray triangle) with equal distance of 2 km. The orange dash line with arrowhead indicates the counter-clockwise wagging direction. (c) P-waves calculated at the virtual stations in (a). (b) Cross-correlation functions of P-waves for different station pairs. Different colors correspond to stations that are separated by different time lags. The cross-correlations indicate that there are time-lags other than 0 or $T_o/2$ between stations.

deviates away from these two specific values, the envelopes provide reasonably tight constraints on the wagging eccentricity and direction. If the time-lag reaches value of 0 (equivalent to T_o due to periodicity) or $T_o/2$, 2-D wagging with eccentricity $e = 1$ is implied.

The behavior of the wagging motion can be deduced by comparing two pairs of seismic stations as well. Consider the example of the station pairs E-S and N-E (see Fig. 8a). The sum of the time-lag for the pair E-S and the pair N-E is $\mathrm{Lag}_{E\text{-}S} + \mathrm{Lag}_{N\text{-}E} = T_o/2$ in counter-clockwise wagging, but is $\mathrm{Lag}_{E\text{-}S} + \mathrm{Lag}_{N\text{-}E} = 3T_o/2$ in clockwise wagging, regardless of the eccentricity. When the wagging is circular ($e = 0$), the pairs E-S and N-E have the same time-lag, with values of either $T_o/4$ or $3T_o/4$. When the eccentricity increases, the two time-lags separate, and the difference in their values increases.

5.3. Application to the Redoubt Volcano 2009 eruption

In this section, we show a sample application of our seismic wave analysis to real seismic data, and also a demonstration of how the seismic data are processed and interpreted within the framework of the wagging model. We use the example of the 2009 eruption of Mt Redoubt in Alaska. According to Alaska Volcano Observatory, the first magmatic explosion occurred at 22:34 (local time) on March 22 in 2009, after precursory seismicity that lasted approximately 6 months[1].

The two recent eruptions of Mount Redoubt were both preceded by seismic tremors (Power et al., 1994; Buurman et al., 2012; Power et al., 2013), for which physical models were developed in

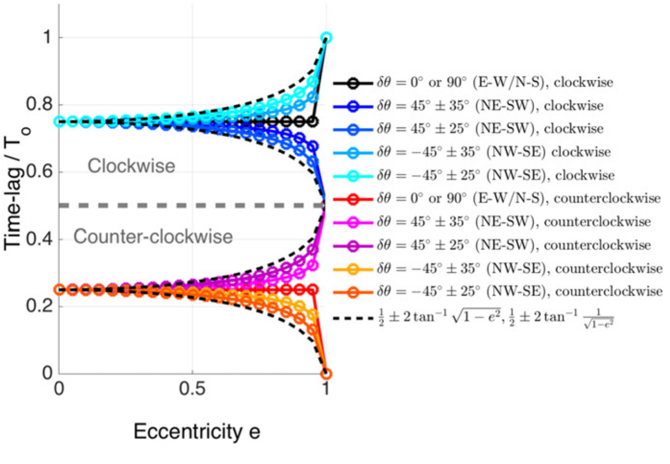

Fig. 9. Time-lag $\mathrm{Lag}_{E\text{-}S}$ between the stations E and S (location in Fig. 8a) as a function of eccentricity of the wagging orbit. Each curve corresponds to a different combination of wagging direction (clockwise or counter-clockwise) and orientation of major elliptical axis (indicated by $\delta\theta$). The upper group of curves (blue to cyan) corresponds to clockwise wagging, and lower group of curves (red to magenta) corresponds to counter-clockwise wagging. When the wagging is in the diagonal direction with tilted major axis at angle $\delta\theta = 45^\circ$ or -45°, the time-lag between the stations reaches its extremum under the same wagging eccentricity. The analytical expression of the extremum values, according to Eq. (32), are shown in black dashed lines, setting the outer boundaries of the time-lags (see Appendix B.2).

---

[2] https://www.avo.alaska.edu/volcanoes/activity.php?volcname=Redoubt&page=basic&eruptionid=610.

previous studies (Chouet et al., 1994; Chouet, 1996; Hotovec et al., 2013; Dmitrieva et al., 2013). Chouet et al. (1994) studied the characteristics of the seismic swarms preceding the 1989–1990 eruption, and proposed a mechanism wherein the resonant excitation of a fluid-driven crack generates long-period seismicity (Chouet et al., 1994; Chouet, 1996). The crack is considered to be a stationary point source of seismicity, and its location and dimensions are determined using seismic data. This model successfully explains some observed seismic features, such as the change in the rate of seismic energy release before the eruption. However, it implies a monopolar seismic radiation, which precludes time-lags between different seismic stations. The 2009 eruption was also preceded by seismic tremor with some unique features. Harmonic tremor with integer overtones was observed, and the fundamental frequency could glide up to as high as 30 Hz in less than 10 min, followed by a seismic quiescence for about 30 s immediately before some explosions. These observations were explained by models invoking the stick-slip mechanism (Hotovec et al., 2013; Dmitrieva et al., 2013). In the model developed by Hotovec et al. (2013), increasingly frequent stick-slip earthquakes give rise to the observed gliding tremor frequency and overtones. Dmitrieva et al. (2013) further developed a frictional faulting model, and proposed that the transition between stick-slip events to aseismic sliding events gives explanation for the observed seismic quiescence before the explosions. Both stick-slip models successfully explained the unique tremor features in the 2009 eruption of Redoubt Volcano, though they may not be readily generalized to other volcanoes which do not display similar seismic characteristics.

These previous studies successfully account for many aspects of seismic observations including the emergence of seismicity, the frequency overtones and the rapid frequency gliding. However, if there are time-lags between the waveforms measured at different stations, they may not be readily explained by either class of models, especially if the time-lag is not static in time, which requires a laterally moving seismic source. Here, we attempt to explain this aspect of seismic characteristics using the more general mechanism of magma wagging, which employs only a few physical parameters, and to test the magma wagging model with the field data as well.

The seismic data used in this study are time series of vertical ground displacement recorded by seismic stations REF, RSO, RDN and RED (Fig. 10). To analyze the time-lags, we select three days (March 10, March 16, and March 21), which are separated by similar intervals (5 and 6 days) for the 2 weeks of the pre-eruptive sequence (the syn-eruptive data on March 22 was avoided due to possible additional complexities during eruptions).

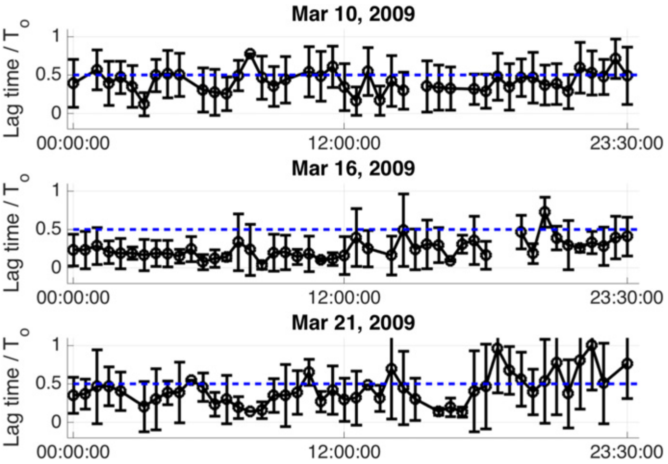
Mar 10, 2009
Mar 16, 2009
Mar 21, 2009

Fig. 11. Evolution of time-lag between stations REF and RSO on March 10th, March 16th and March 21st. The average time-lag calculated in a 10-min window for every 30 min are shown (black circles) with standard deviations (error-bars). The time-lags are normalized by the average oscillation period (obtained from the frequency spectrum). Blue dash lines indicate the value of 1/2 the oscillation period. See Appendix C for details of the data processing.

The waveforms are sampled at a frequency of 100 Hz, and frequencies higher than 5 Hz are filtered out in the post-processing. We choose the seismic station pair REF-RSO, and compute the time-lag $\mathrm{Lag}_{REF\text{-}RSO}$ from the cross-correlation functions (see Appendix C). To obtain meaningful time-lags, the seismic data measured by both stations should have similar waveforms. We impose two selection criteria on the data windows based on frequency spectra and cross-correlation values. First, the frequency spectra of seismic stations REF and RSO must have shared peaks for the data window, reflecting similarity in their frequency content. Second, the peak cross-correlation value between REF and RSO must be sufficiently large (i.e., passing a 95% confident threshold), reflecting similarities in their waveforms. We only compute the time-lags for data windows that pass both tests (see Appendix C).

The time-lags between station REF and RSO have finite values, and show variations in time on certain periods of days (see Fig. 11). Moreover, the time-lags vary smoothly with time for finite time periods (00:00–06:00 on March 16, and 00:00–12:00 on March 21, for

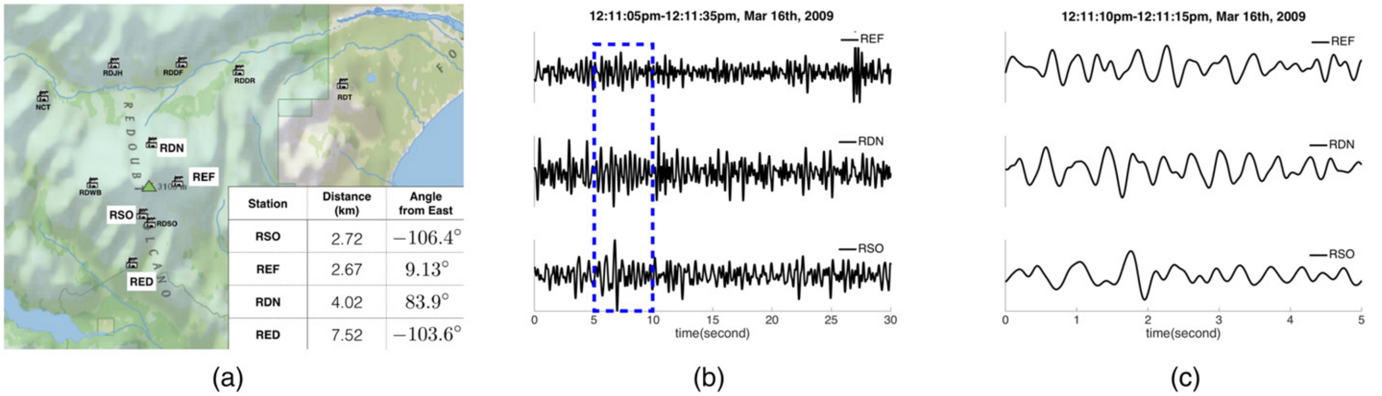

Station	Distance (km)	Angle from East
RSO	2.72	$-106.4°$
REF	2.67	$9.13°$
RDN	4.02	$83.9°$
RED	7.52	$-103.6°$

Fig. 10. (a) Map of Redoubt Volcano and seismic stations RSO, REF, RDN and RED (highlighted). Radial distances to the volcanic vent and angles (measured in the east of north direction) of the highlighted stations are shown in the inset table. Frame (b) shows waveforms recorded by RSO, REF and RDN on March 16th, 2009. Frame (c) shows a 5-s section of the waveforms displayed in the blue rectangle in frame (b). The waveforms in (b) and (c) correspond to the vertical component of the seismograph, from which frequencies higher than 5 Hz are filtered out. Source of data for (a): https://www.avo.alaska.edu/volcanoes/. Source of data for (b) and (c): IRIS.

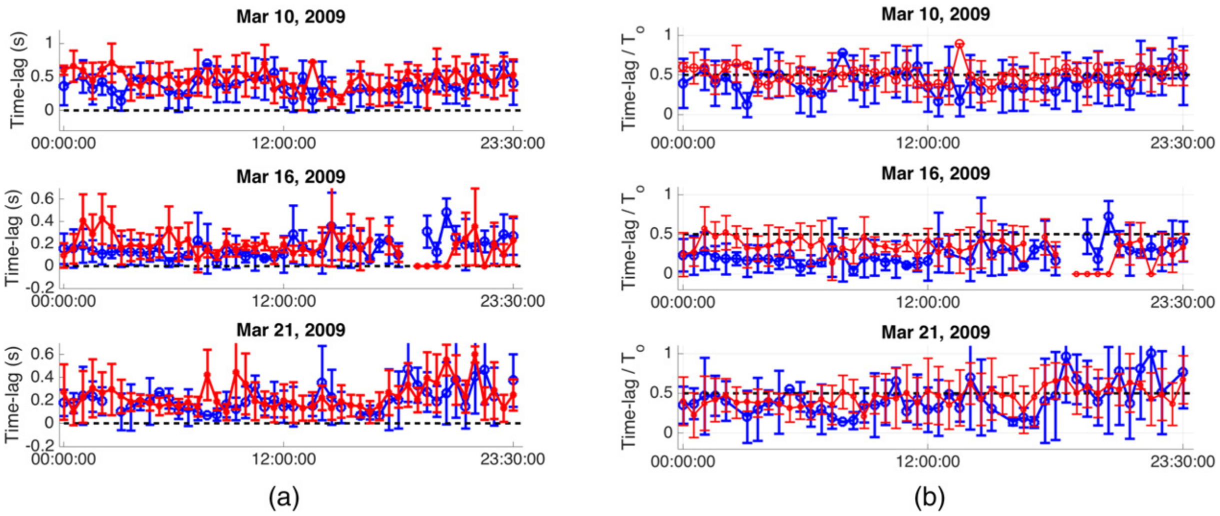

Fig. 12. Evolution of time-lag for station pair REF-RSO and RDN-REF on March 10th, March 16th and March 21st. The time-lag for RDN-REF is corrected based on P-wave velocity $c = 3.5km/s$ for the larger radial distance of RDN (see Appendix D). The average and standard deviation of time-lags are calculated according to the scheme described in Appendix C. The blue curves indicate time-lag for station pair REF-RSO; the red curves indicate time-lag for station pair RDN-REF. The absolute values of the time-lags (in seconds), are shown on the left, and time-lags normalized by period T_o are shown on the right.

example). Although some factors such as the heterogeneity in seismic velocity or specific locations of the seismic stations can contribute to the time-lag, these static properties cannot explain the temporal changes in the time-lag. The temporal dependency of the time-lag, therefore, requires more dynamical explanations. The continuity of time-lags over significant intervals of time indicates that there is a continuously varying source, consistent with a whirling magma column. (Although the data do not yet demand this interpretation.)

Within the magma wagging framework, the time-lags can be interpreted using the diagnostics developed in Section 5.2: for the March 21st record, the time-lag between the two stations fluctuates but stays mostly below $T_o/2$, which indicates, according to Fig. 9 (see also Table 1, Appendix B.2), a highly elliptical counter-clockwise motion with the wagging plane along northeast-southwest direction. For March 16th, the time-lag remains around $T_o/4$ for the first half day, indicating a counter-clockwise wagging with low eccentricity, and a slight increase of eccentricity (or a rotation of the wagging plane) towards the end of the day. For March 21st, the time-lag oscillates between low values to $T_o/2$, indicating counter-clockwise wagging with fluctuating eccentricity (or slow rotation of the wagging plane). Near the end of March 21st, an increase in time-lag suggests a reversal of the wagging direction from counter-clockwise to clockwise (see Fig. 9), although there are significant uncertainties in the time-lag measurements.

We compare the time-lag evolution for station pair REF-RSO to that for RDN-REF, for both their absolute values (Fig. 12a) and normalized values (Fig. 12b). Compared with the range of time-lags on March 10, the ranges of time-lags on March 16 and March 21 have smaller values, suggesting a higher wagging frequency as the volcano approaches eruption. Moreover, the absolute time-lags for both pairs are bounded between 0 and 1 s, indicating sinusoidal waveforms with frequency higher than 1 Hz. Towards the end of March 21st, we observe an increase in time-lags for both pairs from below $T_o/2$ to above $T_o/2$ (see Fig. 12b), indicating a reversal of the wagging direction from counter-clockwise to clockwise.

The wagging model can also be used to interpret statistically significant cross-correlations between multiple stations at different locations, with both different radial distance and angular positions. Fig. 13b shows three cross-correlation functions obtained from four available seismic stations (marked in Fig. 13a), and the analytically calculated cross-correlations of virtual stations located at the same locations for circular wagging. The moderate resemblance between the synthesized and measured cross-correlation functions suggests that circular wagging motion could have occurred one day before the eruption.

Although the Redoubt data suggests features of elliptical wagging motion, there are some inconsistencies between the data and the model's predictions, which warrant more in-depth analysis. Note that the wagging model predicts the sum of the two time-lags to be $\mathrm{Lag}_{E\text{-}S} + \mathrm{Lag}_{N\text{-}E} = T_o/2$ or $3T_o/2$, which is not matched by the measurements (Fig. 12b). The possible explanation for such inconsistency could be that our model assumes a uniform array geometry of seismic stations (equally spaced radially and azimuthally) and a homogeneous seismic velocity field, neither of which is accurate in reality, but can be accounted for to a certain degree (see Appendix D). The difference in vertical elevation between the seismic stations, as well as the mislocation of the magma column, can also introduce errors in the measurements: For example, if the source is off by 500 m and the seismic wave speed is 3–4 km /s, the error introduced by the source mislocation to the time-lag is around 0.15 s(Fig. 16b). As the real seismic data contains irregular sinusoidal waveforms, cycle skipping could introduce errors in the time-lags as well. The simple wagging diagnostics we propose are based on P-wave measurements, however, we utilize the vertical component of ground displacement, which also contains S-waves and Rayleigh waves. It is also worth noticing that eruption was preceded by 58-h seismic swarms, which overlapped the tremor data on March 21, adding some uncertainty to our interpretation (Power et al., 2013).

Despite these limitations, our data analysis suggests that there may exist a moving tremor source in the volcano, which the magma wagging model naturally provides. Over finite periods of time, the time-lags between the station pairs show smooth variation, which is consistent with the model's prediction. The time-lags are further interpreted in the framework of the wagging model, so as to reveal the characteristics of the whirling motion. Although there may be other mechanisms in the 2009 eruption of Mt. Redoubt, the analysis presented above indicates that the motion of the magma column can be detected using field data. At this stage, the model

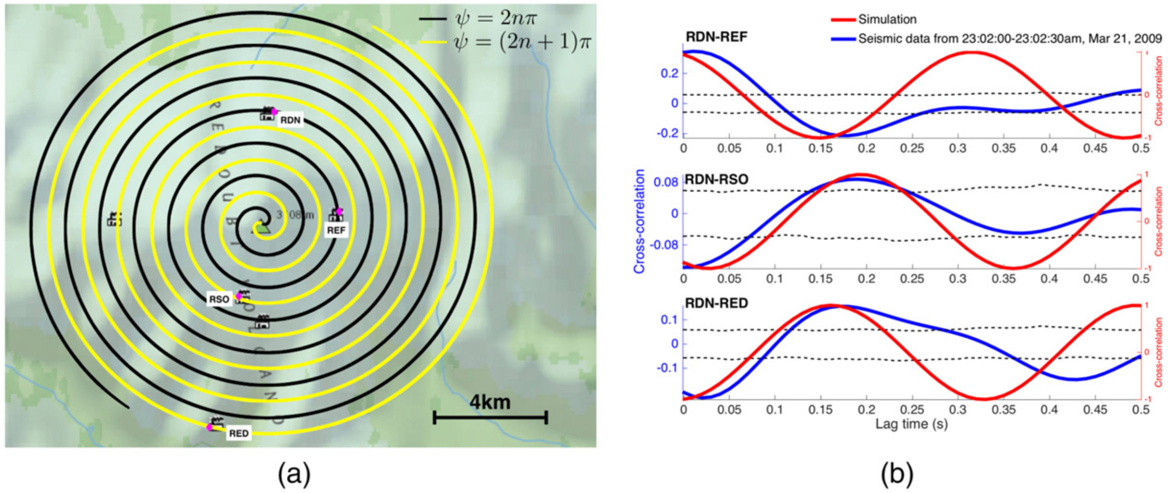

Fig. 13. Radiation pattern for circular wagging that explains the cross-correlations of seismic station pairs with different radial distances. (a) Contours of two phase-shifts calculated by Eq. (30) for a clockwise circular wagging ($e = 0$) with wagging frequency $f = 3$Hz. The seismic velocity $c = 3500m/s$. The reference frame is rotated so that the 0 phase-shift contour (black) overlaps with station RDN. Purple diamonds mark the precise locations of the stations. (b) The cross-correlations calculated from seismic data on March 21st (blue) and predicted by the circular wagging motion (red) described above. Black dashed lines are bounds of upper and lower values of the cross-correlation functions with a > 95% confidence.

is probably too simple to be used for forecasting, or yield definite interpretations of the seismic data. However, the wagging model provides a new framework for analyzing seismic data, and may one day provide better understanding and even forecasting, with further development and testing. The algorithm we proposed in Section 5.2 suggests that a purpose-designed seismic array with specific array geometry (i.e., an array consisting of equal-distance, perpendicularly positioned seismometers) can most efficiently detect the wagging and whirling signal. With future design and deployment of such seismic arrays, the wagging model can be tested with more conclusive findings, and the link between wagging characteristics and the evolution of eruption dynamics can be further interrogated empirically.

6. Discussion

Volcanic tremor is an ubiquitous phenomena common to explosive volcanism across the globe, and plays a critical role in volcanic hazard prediction. Here we extend the magma wagging model (Jellinek and Bercovici, 2011; Bercovici et al., 2013) to higher dimensions, as characterized by the magma column's angular displacement and velocity. The extended model demonstrates that the free-oscillations of the magma column in three dimensions lead to the same fundamental frequency ω_o as in the 2-D model, in the limit of an inviscid magma column. The magma column whirls in the volcano conduit while each of its horizontal section tracks an elliptical orbit, whose eccentricity is determined by the relationship between energy and angular momentum. When the eccentricity of the whirling orbit reaches the maximum value of 1, the 2-D magma wagging model (Jellinek and Bercovici, 2011) is recovered. When viscous damping is present, the whirling motion of an un-coiled magma column is damped at the same decay rate as in the 2-D magma wagging model, while a coiled magma column is damped more rapidly.

We further analyze and predict seismic P-waves generated by magma wagging motion, and suggest a method for probing the motion of the magma column in the conduit using cross-correlations of seismic waveforms. According to our model, the synthesized seismogram contains sinusoidal P-waves in time with frequency ω_o. We propose a diagnostic procedure, by which we can infer the shape of the whirling orbit of the magma column using time-lags of P-waves measured at different locations. A seismic array can be optimally designed to detect the whirling motion of the magma column, when it is comprised of seismic stations separated by 90° and equidistant to the volcanic conduit.

We test our model using data from seismic stations near Redoubt Volcano prior to its eruption in March 2009, and demonstrate how the seismic data are processed and interpreted to allow the detection of a whirling magma column. Our data analysis shows consistency with the wagging model over finite time periods, and suggests that a circular or elliptical wagging motion could have existed for some period of time. The time variation of the time-lags also hints that the wagging direction could have reversed when the eruption was impending; moreover, the wagging eccentricity possibly fluctuates with time. Of course there are other possible mechanisms at play in the 2009 eruption of Mt. Redoubt, and the ground motion observations could be affected by additional complexities (such as seismic swarms preceding the eruption) (Power et al., 2013). Currently, the wagging model is still too simple to be used for forecasting eruptions. However, the preliminary application of the model suggests that the wagging mechanism may one day provide better understanding and even forecasting, with further development and testing.

One important inference from our model is that the evolution of the wagging motion suggested by the seismic data suggests a change in energy and angular momentum of the magma column en route to the eruption. In our model, the wagging eccentricity indicates the ratio of energy to angular momentum. Before an eruption, the increasing rate of gas exsolution and driving force from bubbles in the magma column could contribute to the accumulation of total (kinetic and potential) energy, hence could lead to an increase of eccentricity. Immediately before the eruption, fragmentation of the magma matrix could lead to damage of the gas annulus, causing net torque on the magma column, and modifying the angular momentum. If the net torque is in a direction opposite to the rotation direction of the magma column, a stagnant motion followed by reversal of rotation direction may ensue. These conjectures need to be tested carefully using more seismic data and more in-depth analysis, and the method we propose here opens more possibilities to use seismology to understand the dynamics of volcanic conduits prior to eruptions.

7. Successes, challenges and caveats

The generalized wagging model achieves several goals, including (1) making the original two-dimensional wagging model more robust, leading to prediction of new whirling motions (2) making the wagging mechanism more field-testable by developing a scheme for analyzing and interpreting seismic data and (3) demonstrating how seismic data from the eruption of Mt. Redoubt in 2009 is analyzed and interpreted using the model. The field data show consistency with some predictions of the model, but the complexities of the data suggest that our model is too simple to yield conclusive interpretations. The prediction of the seismic features also suggests that purpose-built seismic array with specific spatial geometry can be optimally designed to test the wagging model.

The wagging mechanism and the seismic diagnostic scheme are based on several assumptions, which warrant scrutiny when complexities of a specific volcanic system is considered. First, the derivation of the whirling motions is based on a long-wave assumption. If a magma column is at the beginning of its unrest, or if the conduit involves small-scale variances (for example, changes in the conduit's geometry and radius, or in the magma's rheology due to gas exsolution) along the vertical direction, then the long-wave assumption will not apply. In this case, the whirling motions and the seismic wavefield caused by the motions will also involve stronger vertical variances, hence require the implementation of a more comprehensive model to incorporate small-scale variances along the z direction. Second, the seismic predictions are based on simplifying the crustal medium, which is assumed to be homogeneous, isotropic, and boundary-free. In reality, the crustal rocks may involve many complexities such as seismic anisotropy and fault boundaries. These effects can render the time-lags sought in the seismic diagnostic scheme unclear or inconsistent. In this case, the seismic diagnostic scheme requires modifications, and more robust data analyzing tools are needed for detecting and picking out the time-lag signals. Other possible tremor mechanisms that can occur concurrently with the whirling of the magma column, such as faulting and fluid migration, can also alter the waveforms, leading to increased difficulty in discerning the effect of a rotational pressure source from other source effects.

Due to the aforementioned complexities that the current model does not yet address, the current model is probably not ready to be directly applied for forecasting eruptions. However, the proof-of-concept model can lead to future developments of more realistic models, which may incorporate more complexities in the system, such as variances in the conduit and magma properties, spacial and temporal evolutions of the gas annulus, tilting and non-cylindrical shape of the conduits, seismic anisotropies and other variances in crustal rocks. Besides the simplifications, the current model also assumes an impermeable gas annulus. Under this condition, the whirling motions are unsustainable and will eventually be damped out by viscous forces. As shown by Bercovici et al. (2013), the incorporation of gas flux through the annulus provides excitation for the two-dimensional wagging motions, suggesting that the incorporation of gas flux in three dimensions may also provide excitations for the whirling motions. This postulation can be further tested by extending the current model that involves a permeable gas annulus, which will be pursued in our future work.

Acknowledgments

This work was supported by the National Science Foundation Grant EAR-1344538 (for Yand Liao and David Bercovici), and by the Natural Sciences and Engineering Research Council of Canada (NSERC) discovery grant (for Mark Jellinek).

Appendix A. Derivation of elliptical trajectories and their periods

For inviscid trajectories governed by Eq. (17), we look for implicit form of solution $u = u(\phi)$. We define $w \equiv 1/u$, in which case the time derivative of u can be written as

$$\frac{du}{dt} = \frac{du}{d\phi}\frac{d\phi}{dt} = \frac{du}{d\phi}\frac{L_o}{u^2} = -L_o\frac{dw}{d\phi} \tag{33}$$

where $L_o = u^2 d\phi/dt$ is the conserved angular momentum. Taking Eq. (33) into the definition of energy,

$$E_o = \frac{1}{2}L_o^2\left(\frac{dw}{d\phi}\right)^2 + \frac{1}{2}L_o^2 w^2 + \frac{1}{2}\frac{\omega_o^2}{w^2} \tag{34}$$

leads to

$$\frac{dw}{d\phi} = \pm\sqrt{\frac{2E_o}{L_o^2} - \frac{\omega_o^2}{L_o^2}\frac{1}{w^2} - w^2} \tag{35}$$

which is integrable and yields the solution

$$\pm\cos 2\phi = \frac{\mathcal{E} - \frac{L_o}{\omega_o u^2}}{\sqrt{\mathcal{E}^2 - 1}} \tag{36}$$

where we assume $\phi = 0$ coincides with the semi-major axis, $\mathcal{E} \equiv E_o/L_o\omega_o$. This solution is readily identified with the relation for an ellipse by taking the transformation $x = u\cos\phi, y = u\sin\phi$, in which case Eq. (36) leads to

$$\frac{x^2}{a^2} + \frac{y^2}{b^2} = 1 \tag{37}$$

where $a^2 = L_o/\omega_o\left(\mathcal{E} - \sqrt{\mathcal{E}^2 - 1}\right), b^2 = L_o/\omega_o\left(\mathcal{E} + \sqrt{\mathcal{E}^2 - 1}\right)$, which is a closed ellipse centered on the centroid (origin), with major and minor axes along the $\hat{x}$ and $\hat{y}$ directions, respectively, and an eccentricity $e = \sqrt{1 - b^2/a^2}$.

To find the periods of the elliptical trajectories, we combine Eq. (19) with $d\phi/dt = L_o/u^2$ to obtain

$$\frac{d\phi}{dt} = \omega_o\left(\mathcal{E} - \sqrt{\mathcal{E}^2 - 1}\cos 2\phi\right) \tag{38}$$

For the closed trajectory, the period T_o, or time needed to complete one revolution, is given by

$$\begin{aligned} T_o &= \frac{1}{\omega_o}\int_0^{2\pi}\frac{\mathrm{d}\phi}{\mathcal{E} - \sqrt{\mathcal{E}^2 - 1}\cos 2\phi} \\ &= \frac{4}{\omega_o}\int_0^{\infty}\mathrm{d}\tan^{-1}\left(\sqrt{\frac{\mathcal{E} + \sqrt{\mathcal{E}^2 - 1}}{\mathcal{E} - \sqrt{\mathcal{E}^2 - 1}}}\eta\right) \\ &= \frac{2\pi}{\omega_o} \end{aligned} \tag{39}$$

Therefore, all elliptical trajectories have period of $2\pi/\omega_o$, which is the same as the period of the steady circular trajectory.

Appendix B. Seismic signatures of magma wagging

B.1. Seismic waves generated by magma wagging

The general solution of the wave Eq. (25) in cylindrical-polar coordinates is a superposition of cylindrical harmonics, usually represented by the two kinds of Bessel functions. The full solution is determined by a full set of initial conditions and boundary conditions. Waves only result from the pressure change on the conduit wall, thus we seek only wave forms propagating outward. The spatial-temporal variation of such waves can be a combination of $cos\omega tJ_m(kr) + sin\omega tY_m(kr)$ and $sin\omega tJ_m(kr) - cos\omega tY_m(kr)$, where J_m and Y_m are first and second type of Bessel functions of order m, respectively. The waveforms can be verified to be propagating outward, using the asymptotic formulas for large values of r

$$\begin{aligned} J_m(kr) &\sim \sqrt{\frac{2}{\pi kr}} \cos\left(kr - \frac{\pi}{4} - \frac{m\pi}{2}\right) \\ Y_m(kr) &\sim \sqrt{\frac{2}{\pi kr}} \sin\left(kr - \frac{\pi}{4} - \frac{m\pi}{2}\right) \end{aligned} \tag{40}$$

which lead to

$$\begin{aligned} &\cos\omega tJ_m(kr) + \sin\omega tY_m(kr) \sim \sqrt{\frac{2}{\pi kr}} \cos\left(-k(r - ct) + \frac{\pi}{4} + \frac{m\pi}{2}\right) \\ &\quad = f_1\,(r - ct) \\ &\sin\omega tJ_m(kr) - \cos\omega tY_m(kr) \sim \sqrt{\frac{2}{\pi kr}} \sin\left(-k(r - ct) + \frac{\pi}{4} + \frac{m\pi}{2}\right) \\ &\quad = f_2\,(r - ct) \end{aligned} \tag{41}$$

which are both waves propagating outward with wave speed $c = \omega/k$. The propagating pressure wave therefore takes the form of

$$\begin{aligned} \Pi(r, \theta) = &\Sigma_m \int_k \cos(m\theta)\,(a_m\,(\cos(\omega_k t)J_m(kr) + \sin\omega_k tY_m(kr)) \\ &+b_m\,(\sin(\omega_k t)J_m(kr) - \cos\omega_k tY_m(kr))) \\ &+ \sin(m\theta)\,(c_m\,(\cos(\omega_k t)J_m(kr) + \sin(\omega_k t)Y_m(kr)) \\ &+d_m\,(\sin(\omega_k t)J_m(kr) - \cos(\omega_k t)Y_m(kr)))\,\mathrm{d}k \end{aligned} \tag{42}$$

which ensures outward traveling waves. When the wagging is counter-clockwise, the inviscid wagging trajectory can be described by $x = a\cos(\omega_o t)$, $y = b\sin(\omega_o t)$, which leads to the boundary condition (27). Retaining modes with angular order $m = 1$, frequency $\omega_k = \omega_o$ and wave length $k = \omega_o/c$, the solution becomes

$$\begin{aligned} \Pi(r, \theta, t) = &\cos(\omega_o t)\cos\theta \left(a_1 J_1\left(\frac{\omega_o}{c} r\right) - b_1 Y_1\left(\frac{\omega_o}{c} r\right)\right) \\ &+ \sin(\omega_o t)\sin\theta \left(c_1 Y_1\left(\frac{\omega_o}{c} r\right) + d_1 J_1\left(\frac{\omega_o}{c} r\right)\right) \\ &+ \sin(\omega_o t)\cos\theta \left(a_1 Y_1\left(\frac{\omega_o}{c} r\right) + b_1 J_1\left(\frac{\omega_o}{c} r\right)\right) \\ &+ \cos(\omega_o t)\sin\theta \left(c_1 J_1\left(\frac{\omega_o}{c} r\right) - d_1 Y_1\left(\frac{\omega_o}{c} r\right)\right) \end{aligned} \tag{43}$$

The coefficients satisfy the inner boundary condition (27), so that

$$\begin{cases} a_1 J_1\left(\frac{\omega_o}{c} R_c\right) - b_1 Y_1\left(\frac{\omega_o}{c} R_c\right) = & \frac{a\rho_o c_g^2}{U\Phi_o} \\ c_1 Y_1\left(\frac{\omega_o}{c} R_c\right) + d_1 J_1\left(\frac{\omega_o}{c} R_c\right) = & \frac{b\rho_o c_g^2}{U\Phi_o} \\ a_1 Y_1\left(\frac{\omega_o}{c} R_c\right) + b_1 J_1\left(\frac{\omega_o}{c} R_c\right) = & 0 \\ c_1 J_1\left(\frac{\omega_o}{c} R_c\right) - d_1 Y_1\left(\frac{\omega_o}{c} R_c\right) = & 0 \end{cases} \tag{44}$$

The solution of Eq. (5) is determined with

$$\begin{cases} a_1 = & \frac{a\rho_o c_g^2}{U\Phi_o}\frac{J_1\left(\frac{\omega_o}{c}R_c\right)}{J_1\left(\frac{\omega_o}{c}R_c\right)^2+Y_1\left(\frac{\omega_o}{c}R_c\right)^2} \\ b_1 = & -\frac{a\rho_o c_g^2}{U\Phi_o}\frac{Y_1\left(\frac{\omega_o}{c}R_c\right)}{J_1\left(\frac{\omega_o}{c}R_c\right)^2+Y_1\left(\frac{\omega_o}{c}R_c\right)^2} \\ c_1 = & \frac{b\rho_o c_g^2}{U\Phi_o}\frac{Y_1\left(\frac{\omega_o}{c}R_c\right)}{J_1\left(\frac{\omega_o}{c}R_c\right)^2+Y_1\left(\frac{\omega_o}{c}R_c\right)^2} \\ d_1 = & \frac{b\rho_o c_g^2}{U\Phi_o}\frac{J_1\left(\frac{\omega_o}{c}R_c\right)}{J_1\left(\frac{\omega_o}{c}R_c\right)^2+Y_1\left(\frac{\omega_o}{c}R_c\right)^2} \end{cases} \tag{45}$$

Note that when the wagging is clockwise, P-waves still have the general form of Eq. (3), but the inviscid trajectory of magma column becomes $x = a\cos(\omega_o t)$, $y = -b\sin(\omega_o t)$. It is also straightforward to show that the P-waves generated by clockwise wagging is equivalent to the P-waves described by Eq. (4) under transformation $\theta \rightarrow -\theta$. When the orientation of the long axis of the elliptical wagging orbit is tilted by $\delta\theta$ from the $\hat{x}$ axis in the counter-clockwise direction, the P-waves generated by the tilted counter-clockwise wagging are obtained by performing the transformation $\theta \rightarrow \theta - \delta\theta$ to Eq. (4); the P-waves generated by the tilted clockwise wagging are obtained by a combination of two transformations that lead to $\theta \rightarrow -(\theta - \delta\theta)$. Define

$$\begin{aligned} \sin\psi_\theta &= \frac{\pm b\sin(\theta-\delta\theta)}{\sqrt{a^2\cos^2(\theta-\delta\theta)+b^2\sin^2(\theta-\delta\theta)}} \\ \cos\psi_\theta &= \frac{a\cos(\theta-\delta\theta)}{\sqrt{a^2\cos^2(\theta-\delta\theta)+b^2\sin^2(\theta-\delta\theta)}} \\ \sin\psi_r &= \frac{J_1\left(\frac{\omega_o}{c}R_c\right)Y_1\left(\frac{\omega_o}{c}r\right)-Y_1\left(\frac{\omega_o}{c}R_c\right)J_1\left(\frac{\omega_o}{c}r\right)}{\sqrt{\left(J_1\left(\frac{\omega_o}{c}R_c\right)^2+Y_1\left(\frac{\omega_o}{c}R_c\right)^2\right)\left(J_1\left(\frac{\omega_o}{c}r\right)^2+Y_1\left(\frac{\omega_o}{c}r\right)^2\right)}} \\ \cos\psi_r &= \frac{J_1\left(\frac{\omega_o}{c}R_c\right)J_1\left(\frac{\omega_o}{c}r\right)+Y_1\left(\frac{\omega_o}{c}R_c\right)Y_1\left(\frac{\omega_o}{c}r\right)}{\sqrt{\left(J_1\left(\frac{\omega_o}{c}R_c\right)^2+Y_1\left(\frac{\omega_o}{c}R_c\right)^2\right)\left(J_1\left(\frac{\omega_o}{c}r\right)^2+Y_1\left(\frac{\omega_o}{c}r\right)^2\right)}} \\ \Pi_{\max}(r,\theta) &= \frac{\rho_o C_g^2}{U_m\Phi_o}\sqrt{\frac{J_1\left(\frac{\omega_o}{c}r\right)^2+Y_1\left(\frac{\omega_o}{c}r\right)^2}{J_1\left(\frac{\omega_o}{c}R_c\right)^2+Y_1\left(\frac{\omega_o}{c}R_c\right)^2}}\sqrt{a^2\cos^2\theta+b^2\sin^2\theta} \end{aligned} \tag{46}$$

in which the + and − stand for counter-clockwise and clockwise wagging, respectively, with tilting angle $\delta\theta$ (see Fig. 14. The solution (4) at specific point (r,θ) can be expressed as

$$\Pi(r,\theta,t) = \Pi_{\max}\cos\left(\omega_o t - \psi_r - \psi_\theta\right) \tag{47}$$

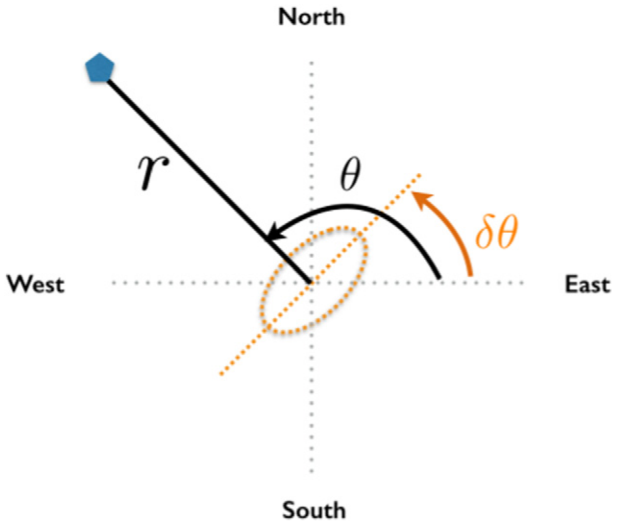

Fig. 14. Sketch of an elliptical wagging orbit, wagging plane (orange dash line) with tilt angle $\delta\theta$ from $\hat{x}$ (the just east direction), and an arbitrary seismic station located at (r,θ).

B.2. *Time-lag between a station pair*

The seismic P-waves generated by magma wagging and recorded by seismic station A and B are $\Pi^{(A)} = \Pi^{(A)}_{\max}\cos\left(\omega_o t - \psi_r^{(A)} - \psi_\theta^{(A)}\right)$ and $\Pi^{(B)} = \Pi^{(B)}_{\max}\cos\left(\omega_o t - \psi_r^{(B)} - \psi_\theta^{(B)}\right)$ according to Eq. (8). When A and B are located at the same radial distance $r^{(A)} = r^{(B)}$, the time-lag $\mathrm{Lag}_{B\text{-}A}$, defined by the time it takes for the displacement peak to travel from A to B, is $\mathrm{Lag}_{B-A} = \psi_\theta^{(B)}/\omega_o - \psi_\theta^{(A)}/\omega_o$. To quantify the relation between the time-lag between a pair of stations to the wagging manner, we use an example of a station pair consisting of two virtual seismic stations, station S and E. The two stations have the same radial distance $r^{(S)} = r^{(E)}$, and are located to the south and to the east of the volcano with $\theta^{(S)} = -\pi/2$ and $\theta^{(E)} = 0$. When the magma column undergoes a counter-clockwise wagging with a tilting angle $\delta\theta = +45^\circ$ from the east direction (wagging oriented in the northeast-southwest direction), the phase-shift $\psi^{(S)}$ and $\psi^{(E)}$ are calculated by Eq. (7), and the difference between the two angles can be expressed as $\psi_\theta^{(E)} - \psi_\theta^{(S)} = \pi - 2\tan^{-1}\frac{b}{a} = \pi - 2\tan^{-1}\sqrt{1-e^2}$. The time-lag, normalized by the period T_o, becomes $\mathrm{Lag}_{E-S}/T_o = \frac{1}{2} - \frac{1}{\pi}\tan^{-1}\sqrt{1-e^2}$. Eq. (7) can also be used to estimate the range of time-lags corresponding to different combinations of wagging directions and orientations (Table 1). When the wagging trajectory's major axis is tilted 45° from the just east or just north direction ($\delta\theta = \pm 45^\circ$), the time-lags $\mathrm{Lag}_{E-S} = 1/2 - \tan^{-1}\sqrt{1-e^2}/\pi$ for counter-clockwise wagging with northeast-southwest orientation; $\mathrm{Lag}_{E-S} = 1/2 - \tan^{-1}\frac{1}{\sqrt{1-e^2}}/\pi$ for counter-clockwise wagging with northwest-southeast orientation; $\mathrm{Lag}_{E-S} = 1/2 + \tan^{-1}\sqrt{1-e^2}/\pi$ for clockwise wagging with northeast-southwest orientation; and $\mathrm{Lag}_{E-S} = 1/2 + \tan^{-1}\frac{1}{\sqrt{1-e^2}}/\pi$ for clockwise wagging with northwest-southeast orientation. The four values form the maximum and minimum time-lags among all wagging motions with the specific eccentricity e (see Fig. 9).

Table 1
Time-lags between pairs of virtual seismic stations that correspond to different combinations of wagging orientations and directions. The seismic stations (see Fig. 7a) are located to the north (station N), east (station E), and south (station S) of the volcano at the same radial distance. The values of time-lags between perpendicular station pairs (N-E and E-S) provide information about the wagging direction and orientation.

Rotation direction	Orientation of long axis	Time-lag between station E to S	Time-lag between station N to E
Clockwise	Northeast-Southwest	$\frac{1}{2}T_o \le Lag_{E-S} \le \frac{3}{4}T_o$	$\frac{3}{4}T_o \le Lag_{N-E} \le T_o$
	Northwest-Southeast	$\frac{3}{4}T_o \le Lag_{E-S} \le T_o$	$\frac{1}{2}T_o \le Lag_{N-E} \le \frac{3}{4}T_o$
	East-West	$\frac{3}{4}T_o$	$\frac{3}{4}T_o$
	North-South	$\frac{3}{4}T_o$	$\frac{3}{4}T_o$
Counter-clockwise	Northeast-Southwest	$\frac{1}{4}T_o \le Lag_{E-S} \le \frac{1}{2}T_o$	$0 \le Lag_{N-E} \le \frac{1}{4}T_o$
	Northwest-Southeast	$0 \le Lag_{E-S} \le \frac{1}{4}T_o$	$\frac{1}{4}T_o \le Lag_{N-E} \le \frac{1}{2}T_o$
	East-West	$\frac{1}{4}T_o$	$\frac{1}{4}T_o$
	North-South	$\frac{1}{4}T_o$	$\frac{1}{4}T_o$

Appendix C. Procedure for calculating time-lags of waveforms

Here we provide a data processing scheme is applied for the calculation of the evolution of time-lags shown in Fig. 11. Seismic waveforms recorded in March 10th, March 16th and March 21st in 2009 are collected from the IRIS open database, with 48 data sets collected for each day. Each data set consists of vertical components of the seismic measurements in the first 10-min section of every 30-min window during the day. For each 10-min section, a set of time-lags is obtained by sliding a 30-s time window (see Fig. 15a) with a 5 s step along the whole 10 min.

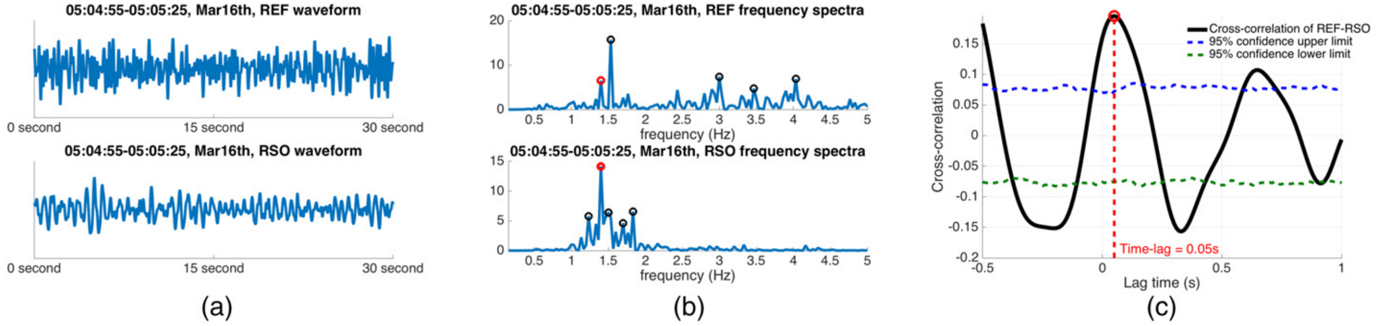

Fig. 15. (a) Waveforms recorded by REF and RSO in a 30 s window on March 16th, 2009. The waveforms have been band-pass filtered between 0.1 Hz and 5 Hz and normalized by their maximum values. (b) Frequency spectra of normalized waveforms shown in (a). Five peaks in the spectra (circles) are selected and compared to identify the shared frequency peak (red circle). When there exists shared frequency peak among for REF and RSO, the waveforms are further filtered to be between [minimum shared frequency $-0.5Hz$, minimum shared frequency $+0.5Hz$], and cross-correlation (c) is computed. The potential time-lag between the station pair is determined to be the positive lag time corresponding to the first peak in the cross-correlation function (red dash line). The 95% confident thresholds (blue and green dash line), following Saar and Manga (2003), Jellinek et al. (2004), are based on an ensemble of 1000 cross-correlation functions, in which each cross-correlation function is calculated with a random phase in each frequency component of one time-series. If the potential time-lag corresponds to a cross-correlation peak above the 95% threshold, the time-lag is considered to be valid.

In order to obtain meaningful time-lags, the seismic data measured by both stations should have similar waveforms. We impose two selection criteria on the data windows based on frequency spectra and cross-correlation values. First, the power spectra of seismic stations REF and RSO must have shared peaks for the data window, reflecting similarity in their frequency content; Second, the peak cross-correlation value between REF and RSO must be large enough (i.e., passing a 95% confident threshold (Saar and Manga, 2003; Jellinek et al., 2004), reflecting similarities in their waveforms. We only compute the time-lags on data windows that pass both tests. For each 30-s window, the frequency spectra of the waveforms recorded by both REF and RSO (Fig. 15b) are computed. Five frequency peaks are found for REF and RSO, respectively (black circles in Fig. 15b). When there exists peak frequency shared by both REF and RSO (red circles in Fig. 15b), the waveforms are further band-pass filtered between the minimum frequency peak and the maximum frequency peak with 0.5 Hz on each end (i.e., if the shared peak frequencies are 1.5 Hz and 2 Hz, the waveforms are further filtered to be between 1–2.5 Hz). The cross-correlation function of the resulting waveforms is computed (Fig. 15c). If the time-lag of these waveforms corresponds to a cross-correlation that exceeds a 95% confidence threshold, the time-lag is adopted into the time-lag data-set. In every 10-min window, the time-lag is the average value of the time-lags measured on all 30-s windows that passed the criteria mentioned above, and the averaged frequency is calculated from the shared frequency peaks in the spectrum of REF and RSO. In the calculation of time-lags shown in Fig. 12, the schemes described above are used on data collected by REF and RDN.

Appendix D. Correction for radial deviation of seismic stations

The diagnostics of wagging motion using cross-correlation of seismic stations discussed in Section 5.2 and Section B.2 apply when the virtual seismic stations are located at the same distance to the imaginary volcano. For the seismic stations in Mount Redoubt, this is not the case. For station pair RDN-REF and REF-RSO, only REF and RSO are similar in radial distance (2.72 km and 2.67 km), but RDN has a much larger radial distance (4.02 km). Comparing with the radial distances, the angular positions of the stations are close to forming 90° pair-wise separations. To use the existing data from RDN, here we correct for the error in cross-correlations between RDN-REF caused by RDN's radial distance, which is 1.35 km larger than that of REF. The P-wave predicted at the desired location r is, according to Eq. (30), $\Pi(r,t)/\Pi_{\max}(r) = cos(\omega_o t - \psi_r(r) - \psi_\theta)$, while the P-wave recorded at the actual location $r+\delta r$ is $\Pi(r+\delta r,t)/\Pi_{\max}(r+\delta r) = cos(\omega_o t - \psi_r(r+\delta r) - \psi_\theta)$. At the specific moment t, the normalized P-wave predicted at r can be obtained by shifting the waveform measured at $r+\delta r$ in time, by the amount of $\delta t = (\psi_r(r+\delta r) - \psi_r(r))/\omega_o$, so as $\Pi(r,t)/\Pi_{\max}(r) = \Pi(r+\delta r, t+\delta t)/\Pi_{\max}(r+\delta r)$. Therefore, when calculating the cross-correlation between station RDN and REF on the time window $[t_1, t_2]$, the waveform measured at RDN on the time window $[t1+\delta t, t2+\delta t]$ should be used. Equivalently, the corrected cross-correlation function can be obtained by shifting the existing cross-correlation function backward by δt. Due to the periodic nature of the waveforms, the relation between δt and δr is also periodic. Within each period, δt is linear with δr (see Fig. 16a). Because the time-lag δt is equivalent to $\delta t + nT_o, (n = 0, 1, 2, \ldots)$, the dependence of δt on δr can be also expressed as $\delta t/T_o = \delta r/\lambda$, where λ is the wavelength, which leads to $\delta t = \delta r/c$, where $c = \lambda/T_o$ is the seismic velocity, which is assumed to be a constant and uniform in our study. To obtain the value of δt, only the seismic velocity is needed, which is a static and measurable value. When $\delta r = 1.35 km$ is corrected for the location of RDN, the cross-correlation function between station RDN and REF is shifted, depending on the seismic velocity (see Fig. 16c). Note that when the P-wave velocity is not precisely known, but is confined in a range of values (for example, from 3km/s to 4km/s (Benz et al., 1996)), the uncertainty in time-lag correction δt increases as δr becomes bigger (see Fig. 16b). Moreover, when $\delta r \ll \lambda$, the wave, while traveling across δr, is less subjected to modifications such as attenuation, scattering, and crustal inhomogeneity. For the station pair RDN-REF, the radial deviation δr is similar, or even larger than the seismic wave length (λ is between 0.7–3.5 km for wagging frequency 1–5Hz). This large deviation could account for the loss of correlation between the seismic stations and lead to sensitive dependence of the corrected cross-correlation function on the seismic velocity (see Fig. 16c). Therefore, it is more difficult to interpret the cross-correlation between stations RDN and REF, when the seismic velocity is subjected to uncertainty. It is worth noting that the mislocation of the magma column itself introduces error in the time-lag measurements as well. The magma column should be reasonably confined to the observable dome structure, and thus if the column mislocation is not excessive, the error caused by the mislocated source is comparable to that caused by a radial variation in the location of any given seismic station. However, if the wagging column is mislocated at a fixed location, the induced error in time-lags would be constant in time; thus the time-varying properties of the time-lags do not reflect source location and can still suggest the changes in wagging motion.

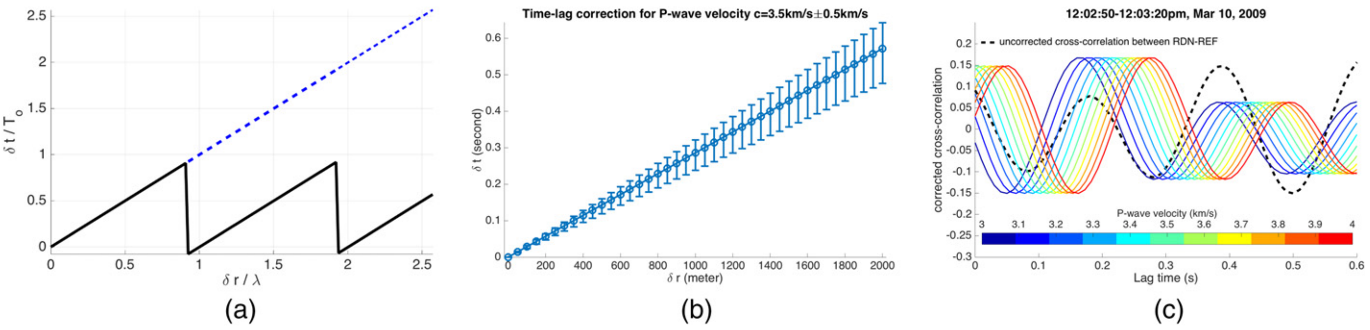

Fig. 16. (a) Shift in time $\delta t = (\psi^{(r)}(r+\delta r) - \psi^{(r)}(r))/\omega_o$ as a function of the shift in radial distance δr (black solid lines) calculated from Eq. (31). δt and δr are normalized by the period T_o and wavelength λ of the seismic wave, respectively. Blue dashed line delineates the linear relationship between δt and δr, which is equivalent to the solid lines due to periodicity in the time-shift. (b) variation of δt when seismic velocity has uncertainty $c = 3.5 km/s \pm 0.5 km/s$. When δr increases, the uncertainly of time-lag correction increases for the same uncertainty in P-wave velocity. (c) Corrected cross-correlation of station pair RDN-REF on a 30-s time window on March 10th, 2009. The corrected cross-correlations (color lines) are calculated based on different P-wave velocities from 3 km/s to 4 km/m. Black dashed line is the uncorrected cross-correlation of P-waves measured by the two stations.

References

Batchelor, G., 1967. An Introduction to Fluid Dynamics. Cambridge Univ. Press, New York.

Benz, H.M., Chouet, B.A., Dawson, P.B., Lahr, J.C., Page, R.A., Hole, J.A., 1996. Threedimensional p and s wave velocity structure of Redoubt Volcano, Alaska. J. Geophys. Res. Solid Earth 101.B4, 8111–8128.

Bercovici, D., Jellinek, A.M., Michaut, C., Roman, D.C., Morse, R., 2013. Volcanic tremors and magma wagging: gas flux interactions and forcing mechanism. Geophys. J. Int. 195 (2), 1001–1022.

Buurman, H., West, M.E., Thompson, G., 2012. The seismicity of the 2009 Redoubt Eruption. J. Volcanol. Geotherm. Res. 259, 16–30.

Chouet, B., 1996. Long-period volcano seismicity: its source and use in eruption forecasting. Nature 380, 309–316.

Chouet, B.A., 1988. Resonance of a fluid-driven crack: Radiation properties and implications for the source of long-period events and harmonic tremor. J. Geophys. Res. 93 (B5).

Chouet, B.A., Matoza, R.S., 2013. A multi-decadal view of seismic methods for detecting precursors of magma movement and eruption. J. Volcanol. Geotherm. Res. 252 (0), 108–175. http://www.sciencedirect.com/science/article/pii/S0377027312003435. https://doi.org/10.1016/j.jvolgeores.2012.11.013. ISSN 0377-0273.

Chouet, B.A., Page, R.A., Stephens, C.D., Lahr, J.C., Power, J.A., 1994. Precursory swarms of long-period events at Redoubt Volcano (1989–1990), Alaska: their origin and use as a forecasting tool. J. Volcanol. Geotherm. Res. 62 (94), 95–135.

Dmitrieva, K., Hotovec-Ellis, A.J., Prejean, S., Dunham, E.M., 2013. Frictional-faulting model for harmonic tremor before Redoubt Volcano eruptions. Nat. Geosci. 6 (8), 652–656.

Garcés, M., Hagerty, M., Schwartz, S., 1998. Magma acoustics and time-varying melt properties at Arenal Volcano, Costa Rica. Geophys. Res. Lett. 25 (13), 2293–2296.

Hotovec, A.J., Prejean, S.G., Vidale, J.E., Gomberg, J., 2013. Strongly gliding harmonic tremor during the 2009 eruption of Redoubt Volcano. J. Volcanol. Geotherm. Res. 259, 89–99. https://doi.org/10.1016/j.jvolgeores.2012.01.001.

Jellinek, A.M., Bercovici, D., 2011. Seismic tremors and magma wagging during explosive volcanism. Nature 470 (7335), 522–525. 02.

Jellinek, A.M., Manga, M., Saar, M.O., 2004. Did melting glaciers cause volcanic eruptions in eastern California? Probing the mechanics of dike formation. J. Geophys. Res. 109 (B9), B09206. https://doi.org/10.1029/2003RG000144.

Julian, B., 1994. Volcanic tremor: nonlinear excitation by fluid flow. J. Geophys. Res. 99 (B6), 11859–11877.

Konstantinou, K., Schlindwein, V., 2003. Nature, wavefield properties and source mechanism of volcanic tremor: a review. J. Volcanol. Geotherm. Res. 119 (1-4), 161–187.

McNutt, S., 2005. Volcanic seismology. Annu. Rev. Earth Planet. Sci. 32, 461–491. https://doi.org/10.1146/annurev.earth.33.092203.122459.

McNutt, S., Nishimura, T., 2008. Volcanic tremor during eruptions: temporal characteristics, scaling and constraints on conduit size and processes. J. Volcanol. Geotherm. Res. 178 (1), 10–18.

Nadeau, P.A., Palma, J.L., Waite, G.P., 2011. Linking volcanic tremor, degassing, and eruption dynamics via SO_2 imaging. Geophys. Res. Lett 38, L01304. https://doi.org/10.1029/2010GL045820.

Neuberg, J., 2000. Characteristics and causes of shallow seismicity in andesite volcanoes. Philos. Trans. R. Soc. London, Ser. A 358 (1770), 1533–1546.

Power, J., Stihler, S., Chouet, B., Haney, M., Ketner, D., 2013. Seismic observations of redoubt volcano, Alaska – 1989–2010 and a conceptual model of the redoubt magmatic system. J. Volcanol. Geotherm. Res. 259,

Power, J.A., Lahr, J.C., Page, R.A., Chouet, B.A., Stephens, C.D., Harlow, D.H., Murray, T.L., Davies, J.N., 1994. Seismic evolution of the 1989–1990 eruption sequence of redoubt volcano, Alaska. J. Volcanol. Geotherm. Res. 64 (1-4), 69–94.

Rust, A., Balmforth, N., Mandre, S., 2008. The feasibility of generating low-frequency volcano seismicity by flow through a deformable channel. Geol. Soc. Lond. Spec. Publ. 307 (1), 45–56. https://doi.org/10.1144/SP307.4.

Saar, M.O., Manga, M., 2003. Seismicity induced by seasonal groundwater recharge at Mt. Hood, Oregon. Earth Planet. Sci. Lett. 214 (3-4), 605–618.

Thompson, G., McNutt, S., Tytgat, G., 2002. Three distinct regimes of volcanic tremor associated with the eruption of Shishaldin Volcano, Alaska 1999. Bull. Volcanol. 64 (8), 535–547.

Unglert, K., Jellinek, M., 2017. Feasibility study of spectral pattern recognition reveals distinct classes of volcanic tremor. J. Volcanol. Geotherm. Res. http://www.sciencedirect.com/science/article/pii/S0377027317301452?via%3Dihub.